SAND REPORT
SAND2003-0166
Unlimited Release
Printed January 2003

Nanostructured Silicon Surfaces for Cost-Effective Photovoltaic Efficiency Improvements

LDRD FINAL REPORT

Douglas S. Ruby, Richard J. Buss, Shanalyn Kemme, and Saleem H. Zaidi

Prepared by
Sandia National Laboratories
Albuquerque, New Mexico 87185 and Livermore, California 94550

Sandia is a multiprogram laboratory operated by Sandia Corporation,
a Lockheed Martin Company, for the United States Department of Energy's
National Nuclear Security Administration under Contract DE-AC04-94-AL85000.

Sandia National Laboratories

Issued by Sandia National Laboratories, operated for the United States Department of Energy by Sandia Corporation.

Available to DOE and DOE contractors from
U.S. Department of Energy
Office of Scientific and Technical Information
P.O. Box 62
Oak Ridge, TN 37831

Telephone: (865)576-8401
Facsimile: (865)576-5728
E-Mail: reports@adonis.osti.gov
Online ordering: http://www.doe.gov/bridge

Available to the public from
U.S. Department of Commerce
National Technical Information Service
5285 Port Royal Rd
Springfield, VA 22161

Telephone: (800)553-6847
Facsimile: (703)605-6900
E-Mail: orders@ntis.fedworld.gov
Online order: http://www.ntis.gov/help/ordermethods.asp?loc=7-4-0#online

SAND2003-0166
Unlimited Release
Printed January 2003

Nanostructured Silicon Surfaces for Cost-Effective Photovoltaic Efficiency Improvements

LDRD FINAL REPORT

Douglas S. Ruby
Photovoltaic System Components Department

Richard J. Buss
Electronic and Optical Materials Department

Shanalyn Kemme
Photonic Microsystems Technology Department

Sandia National Laboratories
P. O. Box 5800
Albuquerque, NM 87185-0753

Saleem H. Zaidi
Gratings, Inc.
Albuquerque, New NM

ABSTRACT

In October 1999, an interdisciplinary team began a three-year LDRD project to study the plasma process of reactive ion etching (RIE). The goal of this work was to evaluate a new regime of plasma surface texturing by using silicon solar cells as an experimental vehicle. Plasma models were developed to explain, predict and guide the plasma texturization process. These models have usefulness in future applications whenever surface texture evolution needs to be better understood and utilized. Optical modeling was also developed to optimize the surface texture required for maximum performance. These optical models developed here should be useful in many of the nanoscale opto-electronic applications currently under development. Additionally, the development of textured surfaces on low-cost multicrystalline silicon (mc-Si) solar cells could significantly advance the photovoltaic industry and potentially enable new thin-film crystalline-silicon approaches that may produce high-power, lightweight, mobile power supplies.

We developed novel metal-assisted texturing processes that produced optically favorable surfaces for solar cells. Large area (~ 200 cm^2), uniform texturing was achieved. Surface contamination and residual RIE-induced damage were removed by incorporation of a complete RCA clean process followed by wet-chemical etching treatments. RIE-textured solar cells with optimized profiles providing performance comparable to wet-chemically etched cells have been demonstrated. A majority of the texture profiles exhibit an enhanced IQE response in the near IR region. The random microstructure represents a superposition of sub-μm grating structures with a wide distribution of periods, depths, and profiles as determined by the SEM measurements.

The optimized texture and damage removal processes were applied to large area (100-132 cm^2) multi-crystalline wafers. Initial results showed improved performance relative to planar, control wafers. However, the texture and solar cell fabrication processes on certain mc-Si materials require further optimization of the RCA clean, DRE treatments, and emitter formation in order to fully realize the benefits of the low-reflection (~ 1-2 %) textured surface.

TABLE OF CONTENTS

INTRODUCTION

The goal of this work was to examine a completely new regime of nanoscale surface texturing for enhancing the performance of silicon solar cells. Nanostructured surfaces can achieve significantly superior optical absorption characteristics compared to conventionally textured surfaces. Such improvements could significantly increase the performance of lower cost multicrystalline silicon (mc-Si) solar cells, and potentially enable new thin-film crystalline-silicon approaches, which could produce high-power, lightweight, mobile power supplies. Using a novel, patent-protected process, we demonstrated excellent texturing of mc-Si using an innovative reactive ion etching technique, and obtained wide-bandwidth spectral reflectance below 1%. The nanoscale texture is robust and well suited for mass production. This interdisciplinary project utilized Sandia's expertise in photovoltaics, plasma processing, sensor-based controls, and process modeling to develop environmentally benign processes that can reduce costs and improve product performance. Large-area commercial silicon solar cells were used as the test vehicle in this program so that improvements in performance can be immediately adopted into mass production. Successful completion of this project also provided validated process models which can be used in a variety of applications for surface texturing, such as to promote adhesion for neutron generator assembly, and potentially to develop quantum-confinement structures to produce long sought-after light-emitting Si diodes.

The quality of low-cost multicrystalline-silicon (mc-Si) has increased to the point that solar cell performance using mc-Si is close to that of single crystal (c-Si) cells, with the major difference resulting from the inability to texture mc-Si affordably. Mc-Si cells are not able to benefit from the cost-effective wet-chemical texturing processes that reduce front surface reflectance on single-crystal wafers because that process relies on the uniform crystalline orientation of c-Si. A low-cost, large-area, random, maskless texturing scheme independent of crystal orientation is expected to significantly impact the cost and performance of mc-Si photovoltaic technology. Web and ribbon-Si technologies also produce high-quality Si wafers, but as yet have not been able to introduce cost-effective cell texturing, which would provide a significant boost in their performance.

The innovation represented by this process lies in its ability to texture entire large-area mc-Si wafers at once. Other novel, wet-chemical approaches that work on some mc-Si materials are not effective on shiny web or ribbon materials because of their lack of nucleation sites. Because the RIE-texturing process removes several microns of material, it may also be used as a replacement for saw-damage removal etching, thereby simplifying and reducing the cost of the wafer preparation process.

We developed a maskless plasma texturing technique for mc-Si cells using Reactive Ion Etching (RIE) that results in higher cell performance than that of standard untextured cells. Elimination of plasma damage has been achieved while keeping front reflectance to low levels. Internal quantum efficiencies higher than those on planar and wet-textured cells have been obtained, boosting cell currents and efficiencies by up to 6% on tricrystalline Si cells.

FIRST YEAR ACCOMPLISHMENTS

We developed several metal-catalyst assisted RIE-texturing techniques using SF_6/O_2 plasma chemistry in a Plasma-Therm 790 reactor. The cathode in the plasma chamber is constructed from graphite while the chamber walls and anode are made of aluminum. A large parameter space of power, pressure, gas ratio, flow rate, and etch time was investigated. A narrow parameter range was found to be useful for texturing Si wafers up to 6" in diameter and mc-Si wafers of 130 cm^2. The textured surfaces exhibit reflectance of between 1 and 5 % for wavelengths below 1 μm without the benefit of anti-reflection films as shown in Figure 1.

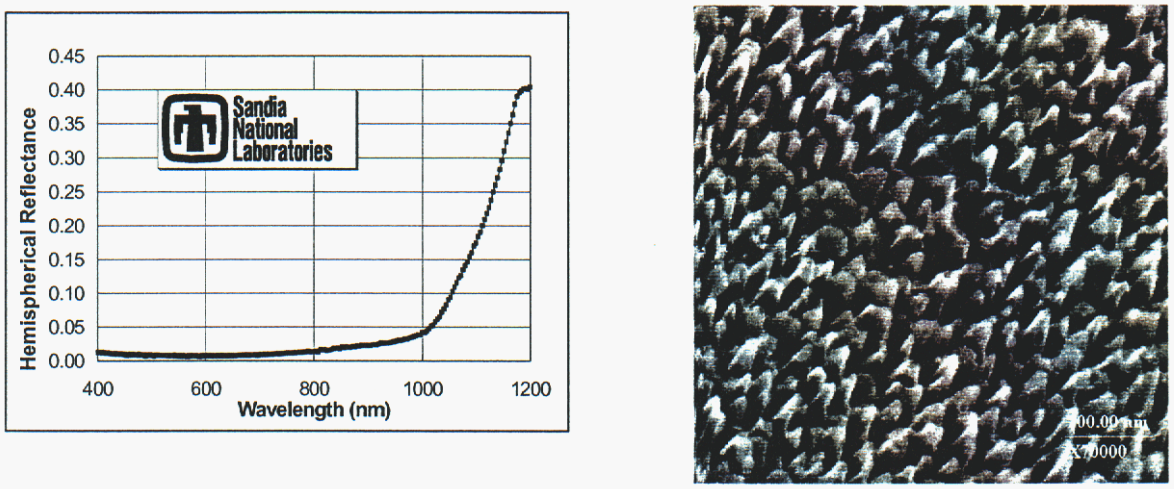

Figure 1. Reflectance and SEM of a mc-Si wafer textured using a Cr-assisted RIE-texturing process.

Solar Cell Development

The challenge involved in incorporating the low-reflectance surfaces obtained from RIE-texturing into a complete solar cell has been to remove the plasma-induced contamination and surface damage without removing too much of the texture. Figure 2 shows the importance of removing all surface contamination before cells undergo phosphorus emitter diffusion.

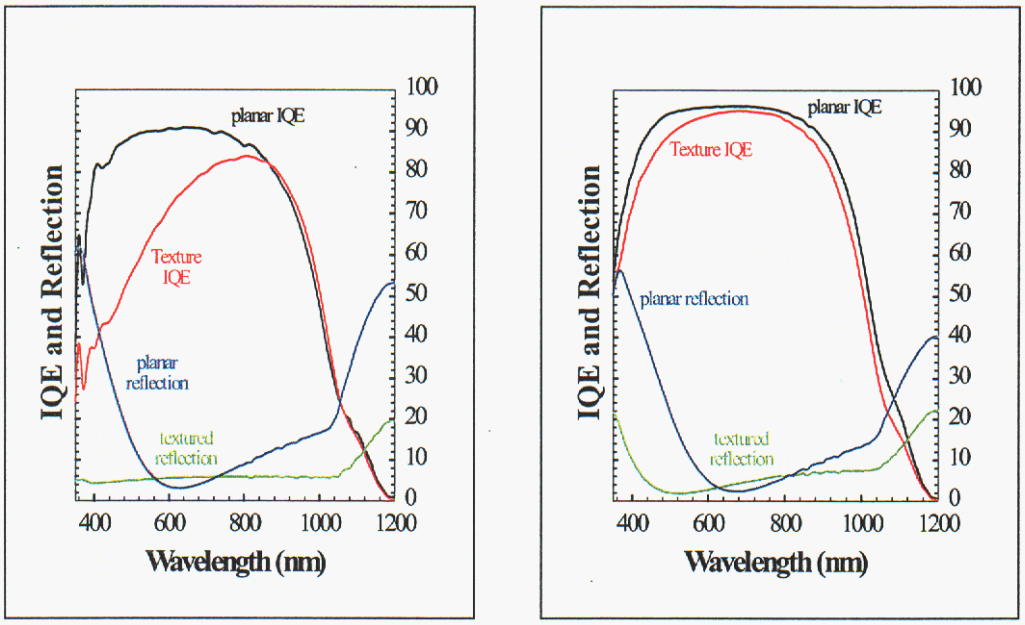

Figure 2. IQE and reflectance of two RIE-textured cells, each with planar and textured regions. The texture process used on the cells was identical, but the cell on the right went through an aggressive RCA cleaning sequence after texturing, while the cell on the left did not.

The IQE of the textured region is lower than that of the planar region even after RCA cleaning, probably due to residual surface damage. Figure 3 shows results of the use of a damage removal etch (DRE) consisting of either KOH or nitric/HF to remove this damaged region.

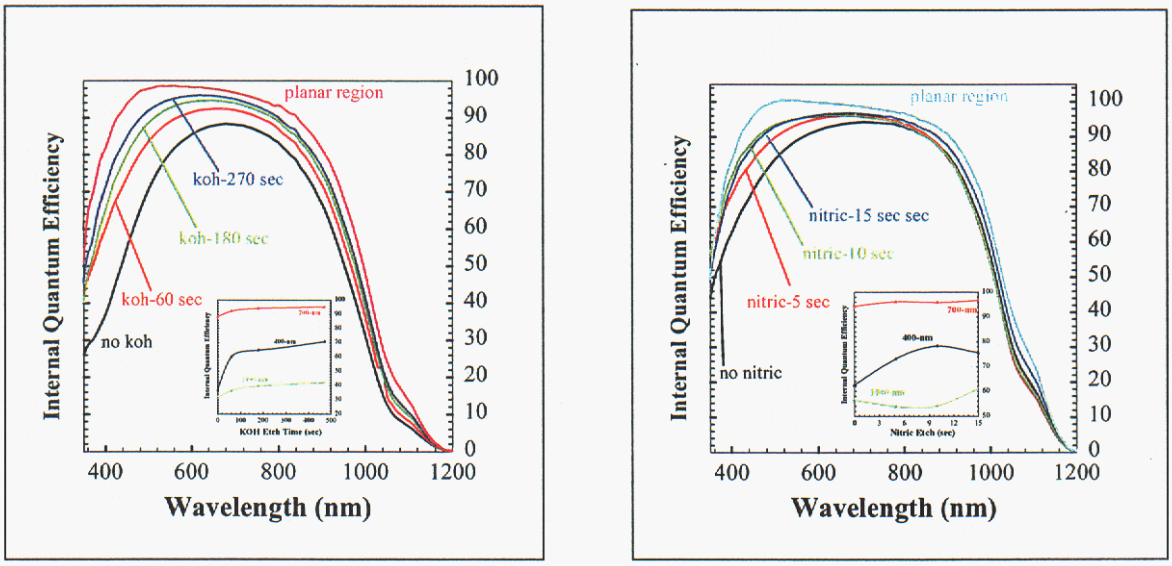

Figure 3. Recovery of textured cell IQE as a function of damage removal etch duration.

With the selection of the proper DRE and RIE-texture processes, we were able to fabricate cells on monocrystalline Si whose IQE was increased to levels as high as that of our best wet-textured cells with reflectances almost as low. The results obtained using an Al-assisted RIE process are shown in Figure 4.

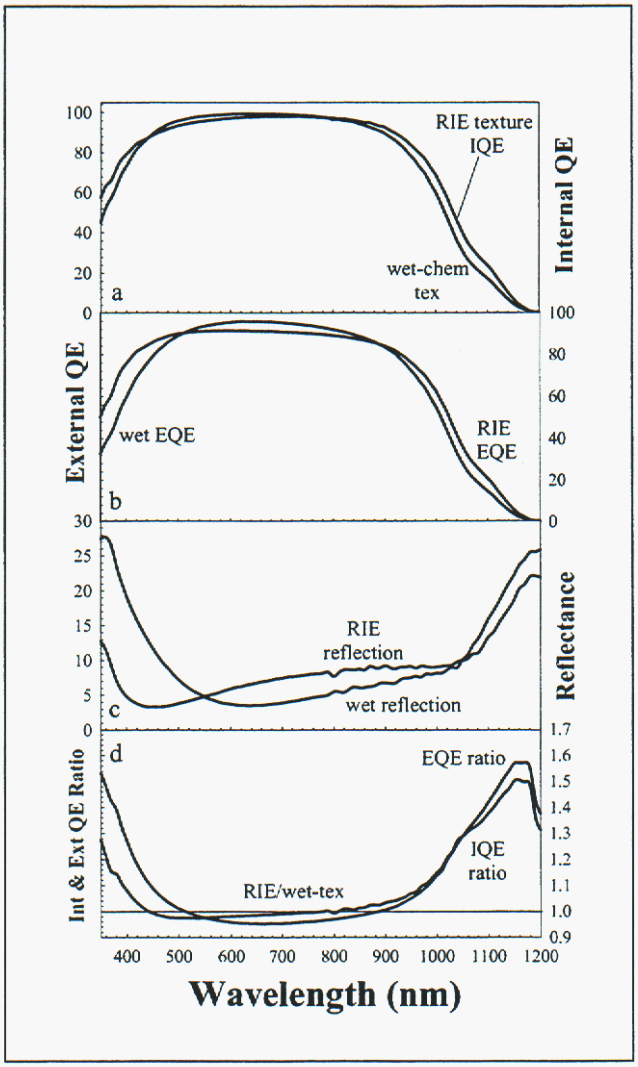

Figure 4.

Graphs a-c show comparisons of IQE, EQE, and hemispherical reflectance of RIE- and wet-textured mono-Si cells, and d shows the RIE/wet ratios of EQE and IQE curves. Because the EQE of the RIE-textured cell exceeds or almost matches that of the wet-textured cell, the Jsc of an RIE-textured cell should match that of the wet-textured cell, and exceed that of a planar cell.

Single-crystal wafers were used to compare the RIE-texturing process to both planar cells, which represent today's untextured mc-Si cells, and to high-efficiency wet-textured cells. The best RIE-textured cells had current densities of over 34.3 mA/cm^2 and efficiencies up to 16.5%, which far exceeded the 31 mA/cm^2 and 14.75% typical of the planar control cells. These results in fact slightly exceeded the average currents and efficiencies of our wet-textured single-crystal control cells, shown in Table 1.

Table 1. Average Illuminated IV Parameters of Mono-Si Cells

Cell surface	Efficiency [%]	J_{SC} [mA/cm^2]	V_{OC} [mV]
Planar	14.8	31.0	615
Wet Texture	16.0	34.0	612
RIE Texture	16.5	34.2	618

The cells in Figure 4 were textured using a process that involved introducing tiny amounts of Al to the SF_6/O_2 plasma. We later developed a different process in which the RIE chamber was pre-conditioned with other metal catalysts, allowing wafers to be textured one after another without having to add metal catalysts each time. Cell results using this process are shown in Figure 5.

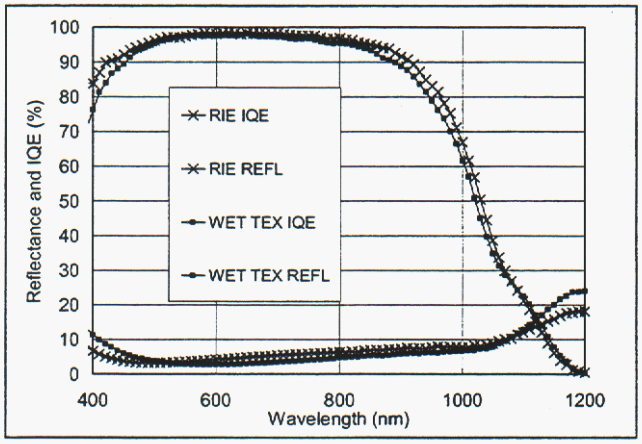

Figure 5. IQE and hemispherical reflectance of mono-Si cells that were wet-textured or RIE-textured using a metal-conditioned chamber.

The superior red-response of the RIE-textured cell shows that no degradation of the bulk diffusion length occurred, even though the metal-assisted texturing was done before the high-temperature diffusion step. This is due to the very thorough RCA cleaning that is done after RIE-texturing. The slight enhancement of RIE-textured red-response may be due to the sub-micron dimensions of the RIE-textured features, which act to diffract some of the incident light into the Si at large angles, promoting better current collection.

The combination of good blue response and low reflectance of the RIE-textured cell shows that all RIE-induced surface damage could be removed while retaining the surface morphology necessary for good absorption. The reflectance obtained with the conditioned texture appears to be even lower than that of the Al-assisted texture, with a AM1.5G spectrum-weighted reflectance of 5.6% that includes reflectance from the gridlines.

These two promising RIE-texture processes were each applied to groups of 12 mc-Si wafers from BP Solarex, and compared with another 12 planar control wafers from the same ingot. Then all wafers were processed through the Solarex cell production line using standard industrial process schedules. The cell performance results are shown below.

Table 2. Average ± Standard Deviation of IV Parameters for 3 Groups of 130-cm^2 mc-Si Cells Processed at Solarex. Average V_{OC} Values were 578 ± 1 mV for all 3 Groups

Cell surface	Efficiency [%]	J_{SC} [mA/cm^2]	FF
Planar	12.0 ± 0.2	28.3 ± 0.1	0.73 ± 0.01
Al-assisted	12.1 ± 0.4	28.6 ± 0.3	0.73 ± 0.02
Conditioned	12.3 ± 0.4	28.6 ± 0.2	0.74 ± 0.02

The average efficiency of the cells with conditioned texture increased 2.5% relative to the planar value due primarily to the higher cell currents. Figure 6 shows reflectance and IQE data for median cells from each of the 3 groups.

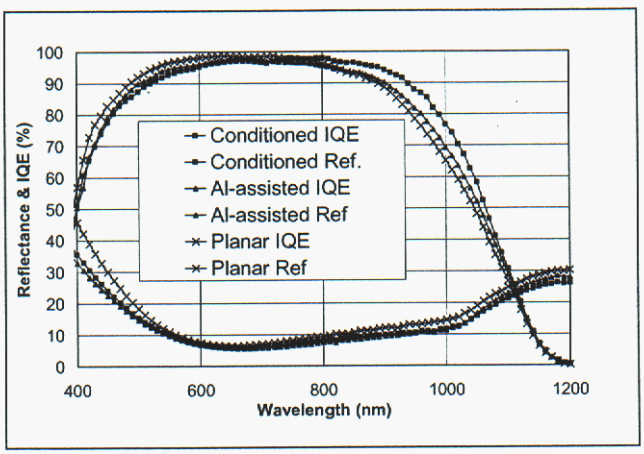

Figure 6. IQE and hemispherical reflectance of 3 mc-Si cells with RIE-textured and planar front surfaces.

The IQEs of the textured cells both show improved red-response due to the oblique light coupling into the Si, especially using the conditioned texture process. The slightly lower blue response is more than compensated for by the lower reflectance at short wavelengths. Both the textured cells show lower reflectance than the planar cell, but not as low as was obtained on mono-Si. This is because a longer-duration nitric/HF DRE was used on these cells to ensure complete damage removal, and this resulted in loss of some of the texture.

One of the advantages of the metal-catalyzed texture process is the ability to obtain different feature shapes and sizes while retaining a wide process parameter window for repeatability. This is shown in Figure 7.

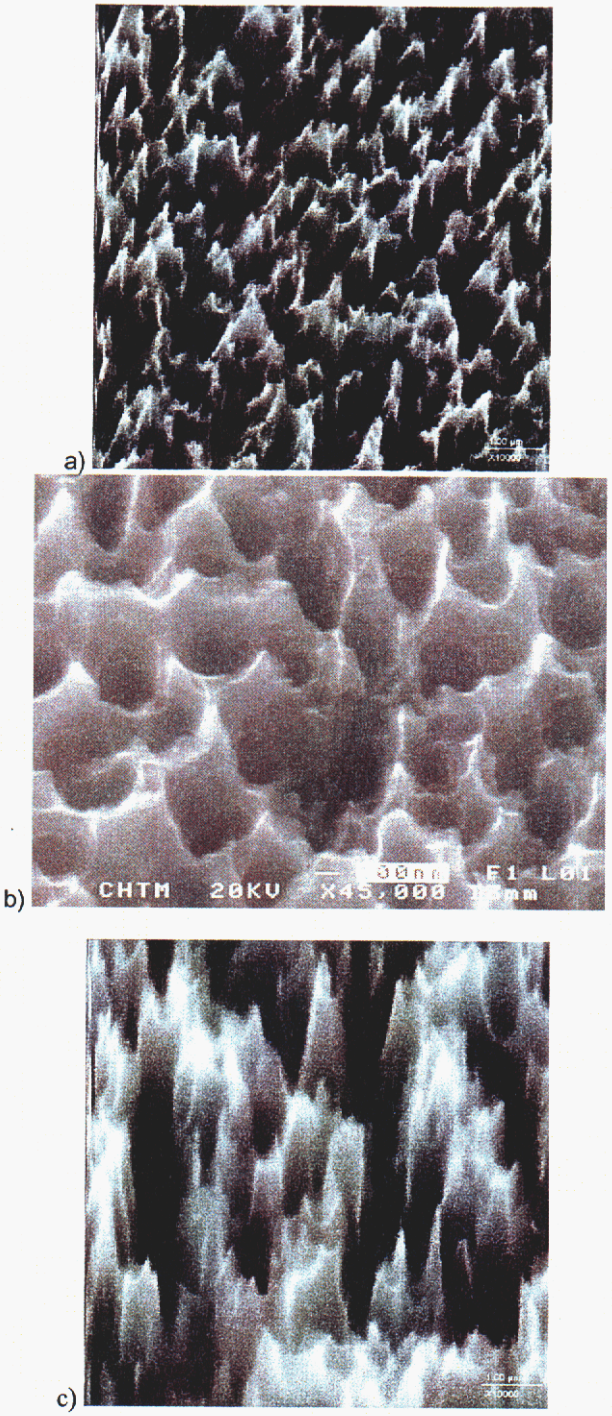

Figure 7. SEMs of textured surfaces using a) conditioned texture, b) Ti-assisted, and c) Al-assisted.

These different morphologies vary the amount of oblique light coupling, resulting in the different textured red-responses of Figure 6, even though the reflectances were similar.

Plasma Modeling

In a previous program which involved uniform plasma etching, we developed a detailed plasma model of the silicon etch process. That plasma etch process used a pure SF6 plasma to remove heavily doped silicon. In the current program, our primary interest is a plasma texturing process where the silicon surface is unevenly etched. The plasma chemistry being used for texturing is an O2 / SF6 mixture. The first goal is the development of a plasma model, which builds on the pure SF6 model by introducing the chemistry of oxygen plasmas. Four species were added to the gas phase, O, O2, O+, and O2+. The electron impact processes, three body recombinations, and some charge exchange reactions of oxygen species were added to the SF6 model. The surface mechanism was altered to include the surface neutralization of oxygen ions and surface recombination of atomic oxygen.

A matrix study of etch rates versus the major process parameters was designed and the first segment of this study has been completed. The model has been refined to produce reasonably good agreement to the experimental results for etch rate versus gas mixture ratio O2/SF6. The calculation does not reproduce the double peak seen in the data. Further refinement of the model will await the acquisition of more measurements. Several elements of the gas phase chemistry have been left out because there is insufficient data to warrant model elaboration. Previous work has demonstrated that SOn species are present in O2/SF6 plasmas, but in order to add the gas phase complexity leading to these species, we would need detailed mass specrometer or laser induced fluorescence measurements to quantify and validate the model.

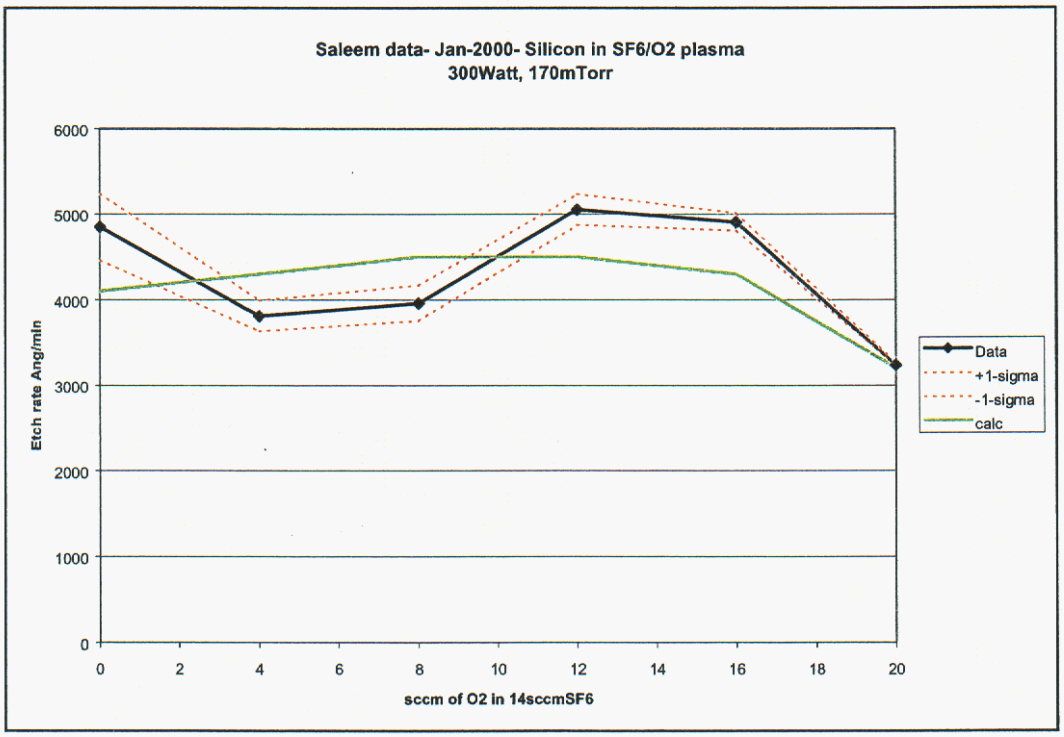

Figure 8. Comparison of plasma etch rate model calculation to experiment.

Optical Modeling

A rigorous coupled wave analysis code, GSOLVER, was used to predict the amount of reflected light from the structured silicon surfaces. These structures were one dimensional, rectangular profile gratings, all with 50% duty cycles. The etch depth and pitch of the gratings were set to match experimental measurements. Each graph also contains a curve showing to the light reflected from a planar silicon wafer, showing an increase at long wavelengths due to reflection off the back sample surface.

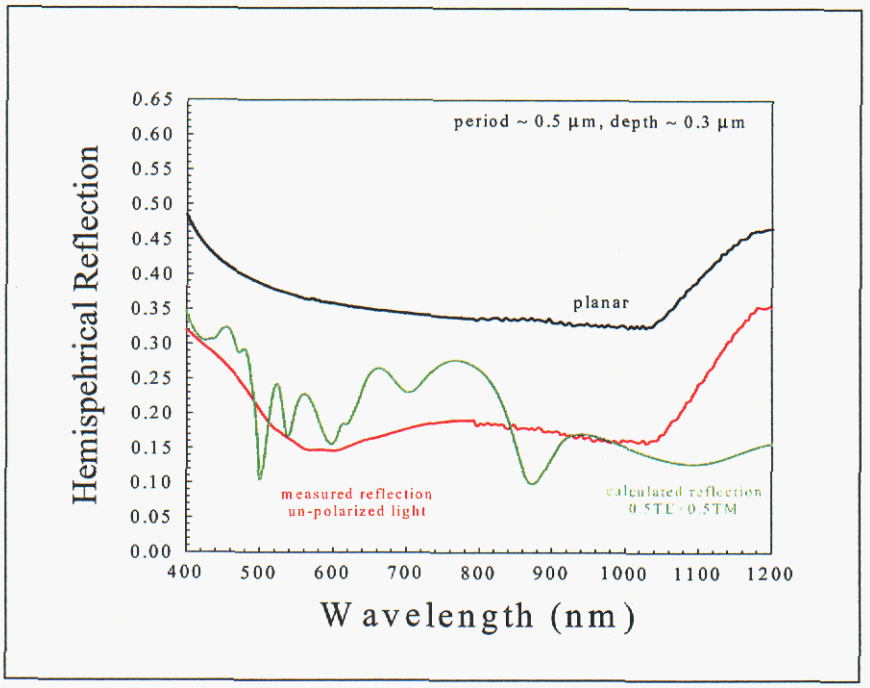

Figure 9. Measured and calculated 1D reflection from 1D 500-nm period Si grating.

SECOND YEAR ACCOMPLISHMENTS

We developed several metal-catalyst assisted RIE-texturing techniques using SF_6/O_2 plasma chemistry in a Plasma-Therm 790 reactor. The textured surfaces exhibit reflectance as low as 1 to 5 % for wavelengths below 1 μm without the benefit of anti-reflection films. We investigated several texturing processes in conjunction with various damage-removal etches (DRE) to determine which produced the highest cell performance for both screen-printed and evaporated metal cell fabrication sequences.

Solar Cell Development

The emitter diffusion was performed by using the dopant oxide solid source (DOSS) process. Source wafers with spin-on dopant applied to both sides were introduced to the furnace together with the samples so that every sample was stacked in front of a source wafer on one side only. This diffusion technique was used to take advantage of the in-situ oxide grown in the same furnace cycle as the phosphorus diffusion. This one-step furnace process leads to phosphorus diffusion, textured, in-situ oxide passivated solar cells that are immediately ready for metallization. Finally, the cells received a single-layer plasma-enhanced chemical vapor deposited (PECVD) silicon-nitride antireflection coating (ARC).

We compared four different metal-assisted texture processes: Al-assisted, Cr-assisted, Ti-assisted, and a chamber-conditioned texture. These were used in conjunction with a dilute acid DRE, a KOH DRE, or no DRE at all. Tables 3 and 4 show the wafer average efficiencies of evaporated-metal and screen-printed cells, respectively. These cells, each 4-cm^2, were measured at Georgia Tech.

Table 3. Wafer Average Efficiency of up to 9 Metal-evaporated Cells

	Acid DRE	**No DRE**	**KOH DRE**
Ti-assisted	14.1	14.2	
Conditioned	14.0	13.7	**12.9**
Al-assisted	13.6	**12.8**	
Cr-assisted	13.8	13.9	

The average of the planar control cells was 13.3%. The cells in **bold** exceeded the efficiency of the controls.

Table 4. Wafer Average Efficiency of up to 9 Screen-printed Cells

	Acid DRE	**No DRE**	**KOH DRE**
Ti-assisted	13.8	**13.2**	
Conditioned	14.0	**12.8**	**13.4**
Al-assisted	13.6	**13.0**	
Cr-assisted	13.8	**12.7**	

The average of these planar control cells was 13.4%. The cells in **bold** exceeded the efficiency of the controls.

For cells that performed better than the controls, most of the improvement was due to increased short-circuit current, with slight additional increases in open-circuit voltage. To investigate this further, we measured the internal quantum efficiency (IQE) and spectral reflectance of median cells from representative groups. Measurements of the Ti-assisted, metal-evaporated cells are shown in Figure 10.

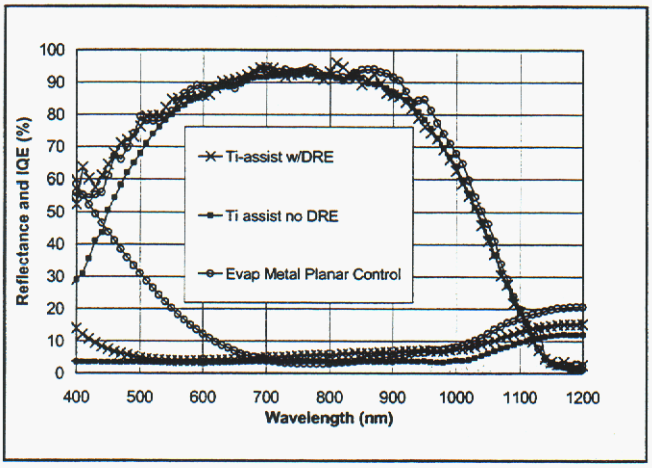

Figure 10. IQE and hemispherical reflectance of three metal-evaporated mc-Si cells.

The Ti-assisted cell without DRE has the lowest reflectance, but suffers from a poor blue-response. The Ti cell with acid DRE has only slightly higher reflectance, but its IQE is as high as that of the planar control cell.

For the screen-printed cells, the process that produced the best results was the conditioned texture process. IQE and reflectance curves of these cells are shown in Figure 11.

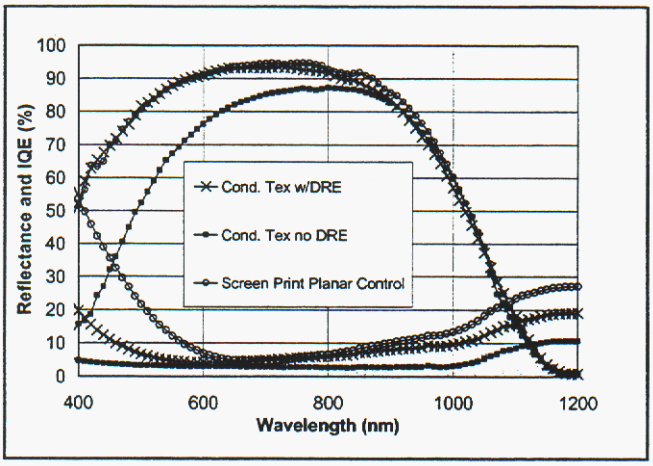

Figure 11. IQE and hemispherical reflectance for three screen-printed mc-Si cells.

Again, the textured cell without DRE has the lowest reflectance, but even poorer blue-response. The IQE of a textured cell is completely restored to that of the planar cell by the DRE with only a slight increase in reflectance.

The RIE-texture process produces extremely low-reflectance surfaces. The solar weighted reflectance of the no-DRE cells in Figures 1 and 2 are 3.6% and 3.4%, respectively, including the reflectance from the gridlines. However, the RIE process causes some shallow surface damage. This results in the recombination of carriers generated by short-wavelength light absorbed near the surface, resulting in low blue-response.

The DRE, consisting of a 10 second dip in a nitric/HF acid mixture, removes the entire damaged region, as indicated by the complete recovery of the IQE to that of the untextured cells. Yet, because so little of the texture is removed, as shown in Figure 12, the solar-weighted reflectance increases to only 5.9% and 7.0% for Ti and conditioned textures, respectively. This compares to 13.0% and 12.8% for metal-evaporated and screen-printed planar cells with a single-layer ARC.

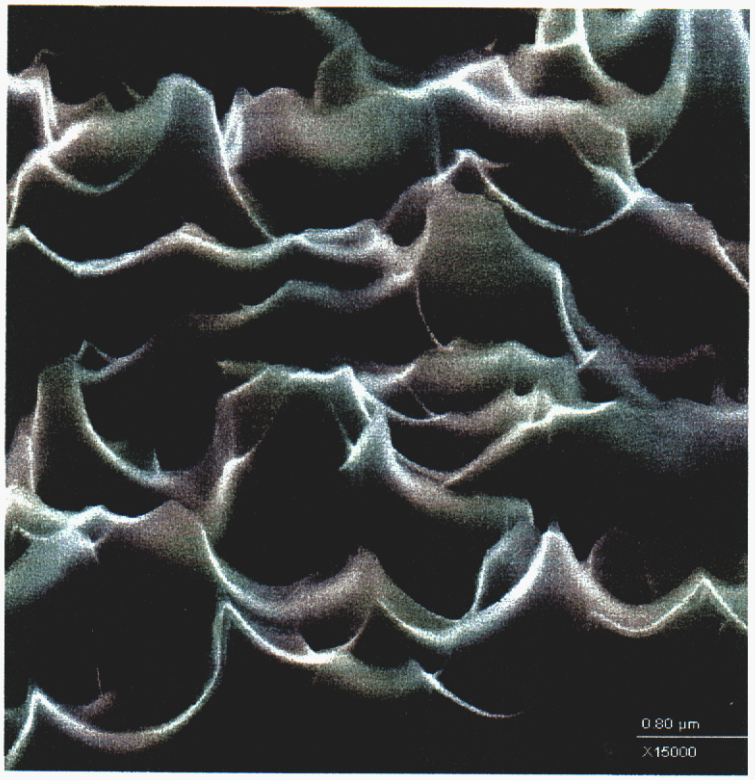

Figure 12. SEM of conditioned-texture cell after acid DRE.

Because the IQE of the Ti-textured cell without DRE is not too low, the metal-evaporated cells with no DRE still outperform the planar controls, and offer some promise that simplified processing without DRE may be possible. Perhaps this is due to the slight surface etching that takes place when oxide is removed just before metal gridline evaporation.

The conditioned RIE process with an acid DRE seemed to offer the largest and most consistent improvements, especially in the important case of screen-printed cells, which will be the most likely use of textured mc-Si. The conditioned texture process will be evaluated further for process simplification, such as shortening of the RCA-clean that precedes the DRE.

This investigation determined that RIE-texturization of mc-Si followed by a short wet-chemical etch can increase the performance above that of planar cells by up to 7% for metal-evaporated and 4% for screen-printed cells, respectively. Typical commercial planar mc-Si cells with a single-layer ARC should be able to use this process to boost their performance.

Plasma Process Modeling

The major process-modeling goal for this year was to develop an ability to simulate and ultimately predict our plasma surface texturing process. Sandia already has code (AURORA) developed for modeling the chemistry of these plasmas and this was used successfully in the first year of this program. We also have code (ICARUS) for direct simulation of 2-D plasma etch. Neither code can simulate topological development on the nano-scale (or on any scale) needed to model the texturing of silicon. We began this year by doing an in-depth study of codes outside Sandia that have topological capabilities. Our conclusion was that nothing available would allow the 3-D simulation with complex gas and surface chemistry needed to fully mesh with our existing codes. We began developing a new code (SURFMOD) which will ultimately take the mechanism developed with AURORA, and interface with ICARUS to simulate surface topography evolution. The code interfaces have not been fully developed yet, but the main architecture is in place and allows simulations of the plasma-texturing process. Figure 13 (left) shows a 3D projection of a 5 micron by 5 micron surface area that has been textured for 60 simulated seconds of plasma etch.

The code allows gas phase species to interact with a surface, either depositing or etching, and allowing the particle surface dynamics to be specified for each species. Thus ions can etch depending on their angle with the surface normal, while neutral radicals may etch isotropically, and each species can have its own kinetics. We think that the texturing effect is the consequence of micromasking by metal atoms or clusters sputtered onto the surface. The code allows a time-dependent deposition of metal clusters on the surface, which leads to significant roughening. We have measured the time behavior of the blackening effect and Figure 13 (right) shows a SEM photo of the developing topography. We can successfully model the early development of fine, 40 nm features, but the subsequent smoothing trend is not possible if the sputtering of micromasking clusters remains constant. Only by adding a time constant for reduction of sputtering do we see the long term smoothing behavior. The process is insufficiently understood at present to know whether this is a valid model. More comparison of model and measurement will help build our confidence in the model.

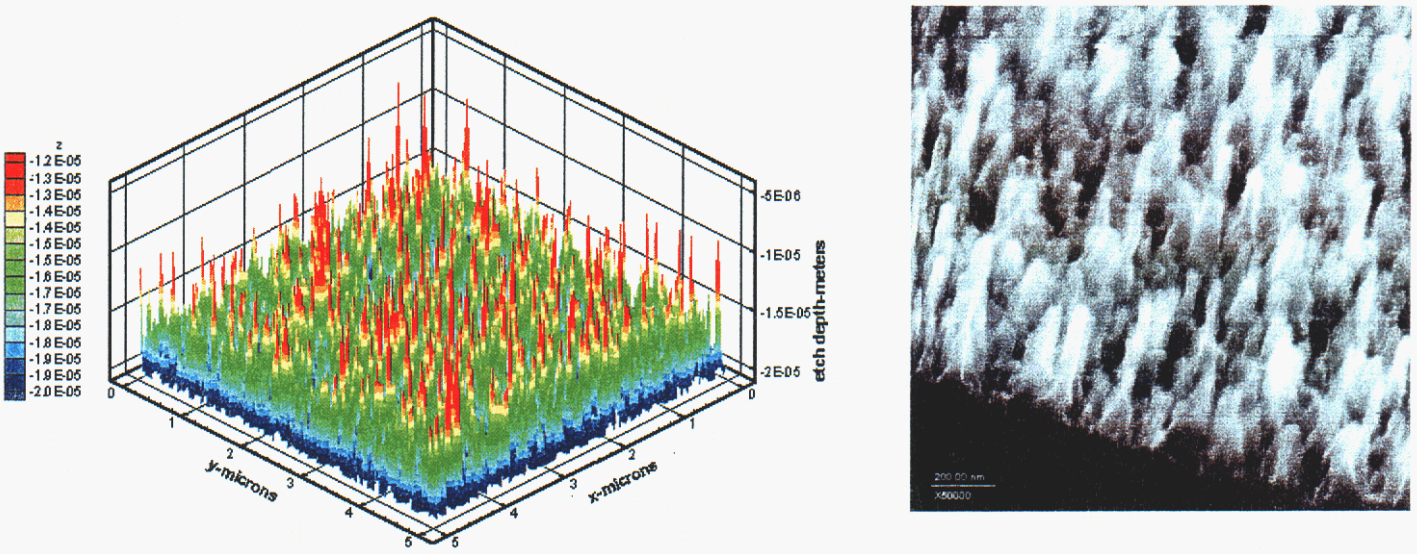

Figure 13. A 3D projection (left) of a 5 micron by 5 micron surface area that has been textured for 60 simulated seconds of plasma etch, (right) SEM photo of textured surface after 50 seconds. The SEM length scale is 200 nm.

Optical Modeling

Modeling Si Grating Zero-Order Spectral Reflectance

Numerical models were utilized to predict the spectral reflectance of various 1D Si gratings. Each grating contained a range of parameters such as grating depth or line width that made simulation with a single grating configuration inappropriate. For this reason, the below simulated results are averages over all combinations of grating parameters represented on the measured grating. For example, the left graph of Figure 14 shows the four spectral reflectance curves corresponding to the grating parameters that appear on one sample. The right graph in Figure 14 give the average of these curves for TE incident light.

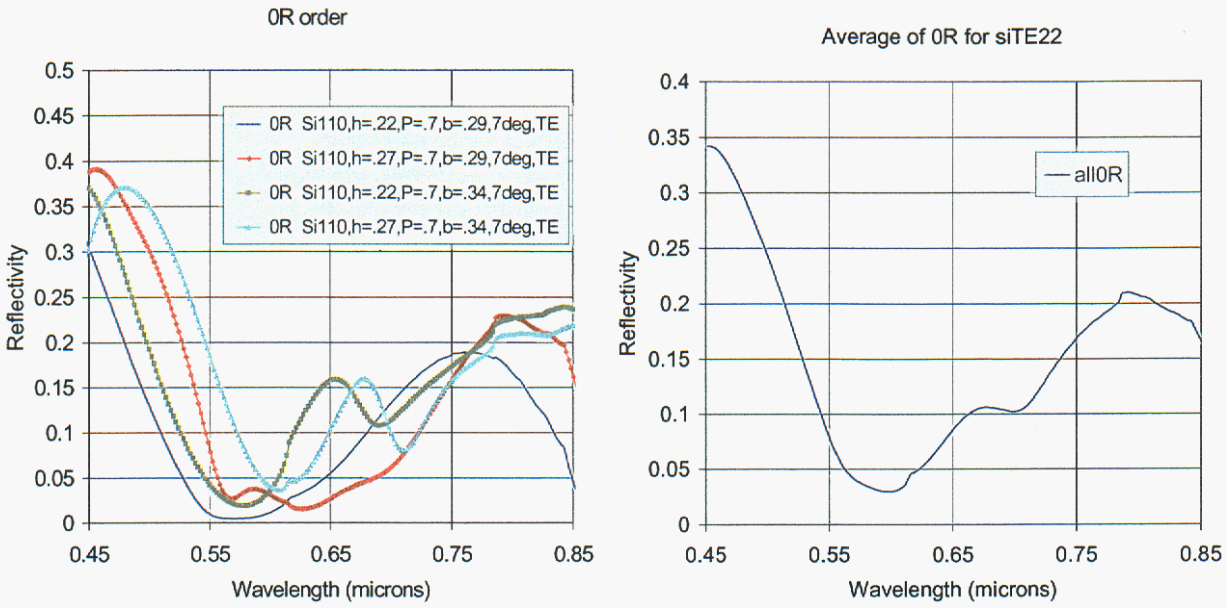

Figure 14. Simulated spectral reflectance curves (left) representing all grating parameter combinations within the measurement: grating depth = 0.22-0.27 μm, grating pitch = 0.7 μm, and line width = 0.29-0.34 μm for TE incident light. Average of the four simulated curves (right). These data are absolute reflectivities and may be compared to measured data that are normalized to an Al mirror as Al has a flat 98% reflectivity across this waveband.

All measurements for this report are performed at a 7 degree incident angle (as opposed to normal incidence). Consequently, the measured reflected signal (the zero order) is also at 7 degrees. Simulations were performed with these same parameters to obtain consistent predictions. The measured spectra in Figures 15 through 17 are normalized to an Al mirror. These measured data may be compared to absolute simulated spectra as Al has a flat 98% reflectivity across this waveband.

The simulated spectra (left) and the measured spectra (right) in Figure 15 appear to be in general agreement in both spectral feature location in the waveband and reflectivity values. Simulated spectra in Figures 16 and 17 show similar reflectivity values but with finer spectral features. However, these simulations do not agree with the very small measured reflectivity values shown in the right graphs of Figures 16 and 17. It is curious that the measured spectral reflectance values would decrease so severely across the wide waveband from the nominal 20% in Figure 15 to the nominal 2% in Figures 16 and 17.

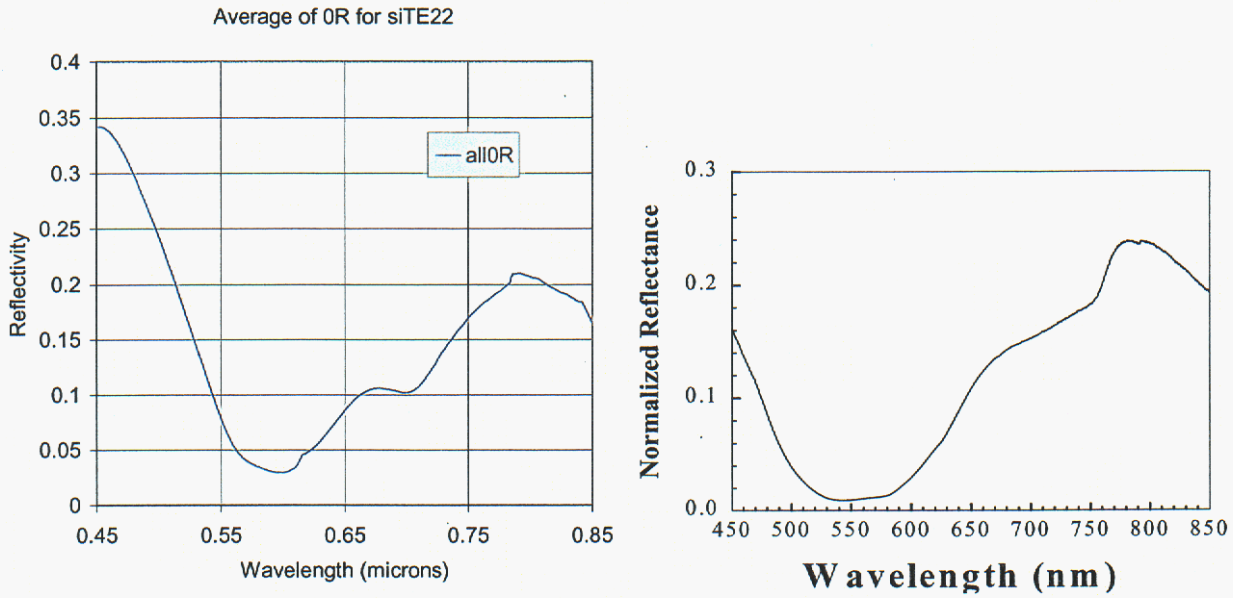

Figure 15. (left) Simulated average spectral reflectance curve representing all grating parameter combinations within the measurement: grating depth = 0.22-0.27 μm, grating pitch = 0.7 μm, and line width = 0.29-0.34 μm for TE incident light. (right) Measured .spectral reflectance curve of the same grating, normalized to an Al mirror.

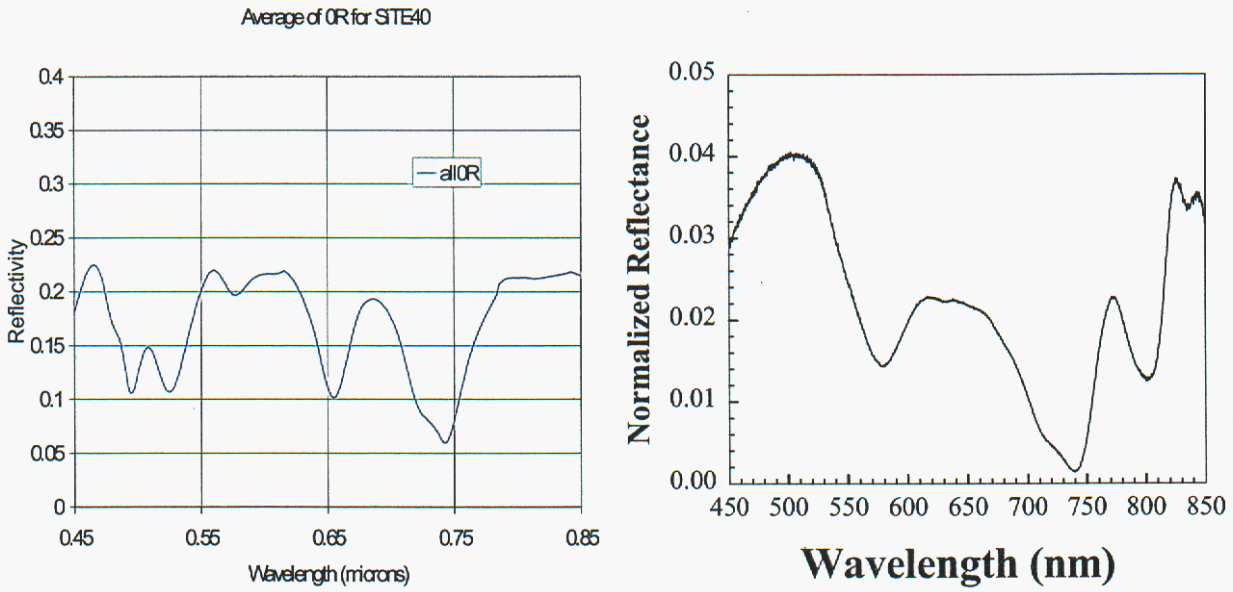

Figure 16. (left) Simulated average spectral reflectance curve representing all grating parameter combinations within the measurement: grating depth = 0.40-0.53 μm, grating pitch = 0.7 μm, and line width = 0.32-0.42 μm for TE incident light. (right) Measured .spectral reflectance curve of the same grating, normalized to an Al mirror.

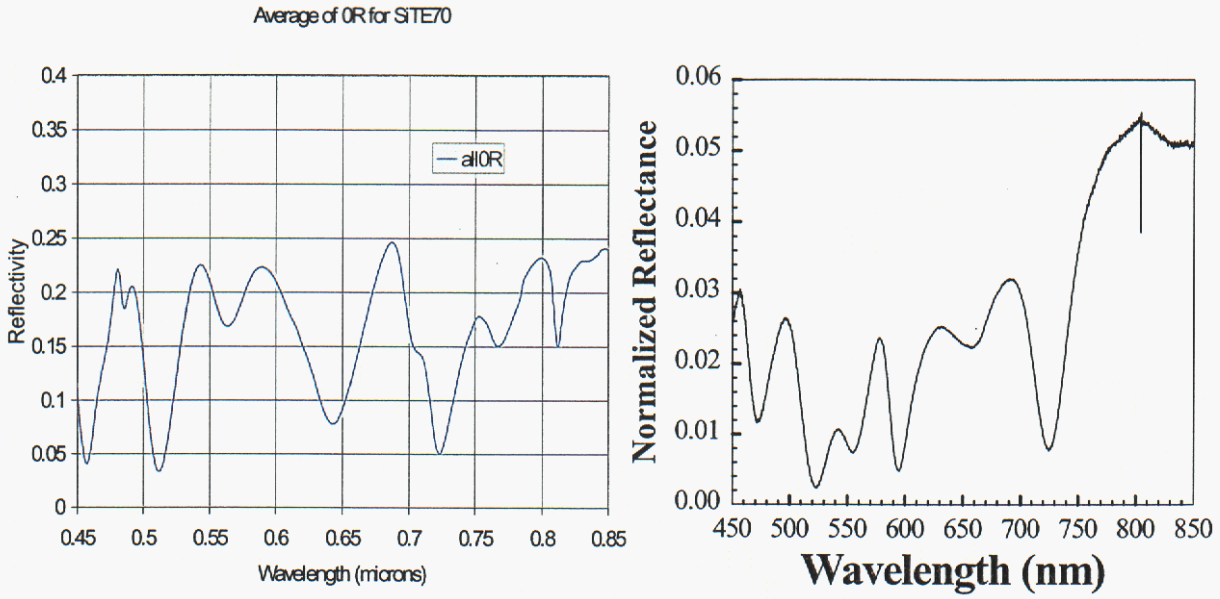

Figure 17. (left) Simulated average spectral reflectance curve representing all grating parameter combinations within the measurement: grating depth = 0.70-0.73 μm, grating pitch = 0.7 μm, and line width = 0.36-0.39 μm for TE incident light. (right) Measured .spectral reflectance curve of the same grating, normalized to an Al mirror.

In addition to the measured spectra shown above, another set of measured spectra were provided from the same grating but this time they were measured relative to a planar Si surface. Figure 18 shows several spectral curves for a planar Si surface for various crystallographic directions. These are all similar and the Si110 curve is used to normalize the simulated responses in Figure 19. These zero-order reflectance measurements were made for both TM and TE incident light. Figure 19 contains the simulated spectra, which should be compared to the measured spectra.

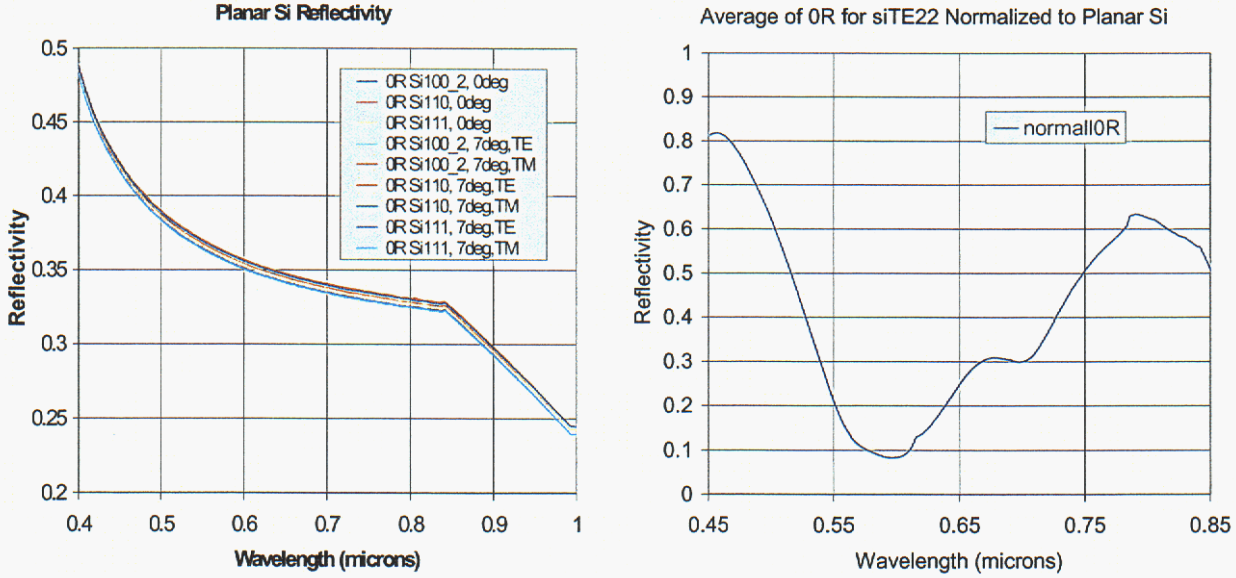

Figure 18. (left) Simulated spectral reflectance curves for several Si crystallographic directions with both TE and TM incident light and 7 degrees and normal incidence. (right) Simulated average normalized spectral reflectance curve representing all grating parameter combinations within the measurement: grating depth = 0.22-0.27 μm, grating pitch = 0.7 μm, and line width = 0.29-0.34 μm for TE incident light. These data are reflectivities normalized to planar Si spectral reflectance curve.

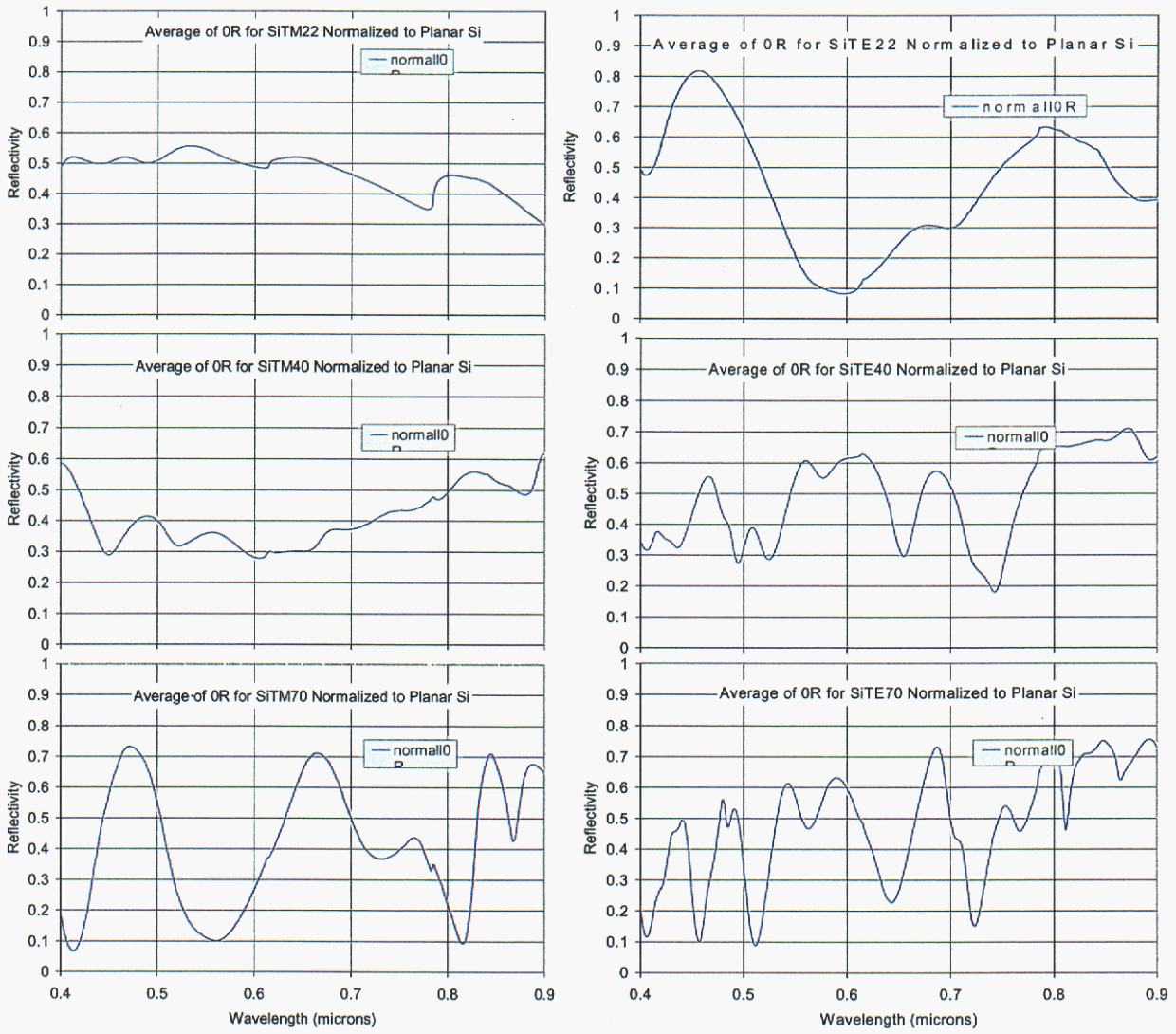

Figure 19. (upper left) Simulated average normalized spectral reflectance curve representing all grating parameter combinations within the measurement: grating depth = 0.22-0.27 μm, grating pitch = 0.7 μm, and line width = 0.29-0.34 μm for TM incident light. (upper right) Same for TE incident light. (mid left) Simulated average spectral reflectance curve representing all grating parameter combinations within the measurement: grating depth = 0.40-0.53 μm, grating pitch = 0.7 μm, and line width = 0.32-0.42 μm for TM incident light. (mid right) Same for TE incident light. (lower left) Simulated average spectral reflectance curve representing all grating parameter combinations within the measurement: grating depth = 0.70-0.73 μm, grating pitch = 0.7 μm, and line width = 0.36-0.39 μm for TM incident light. (lower right) Same for TE incident light.

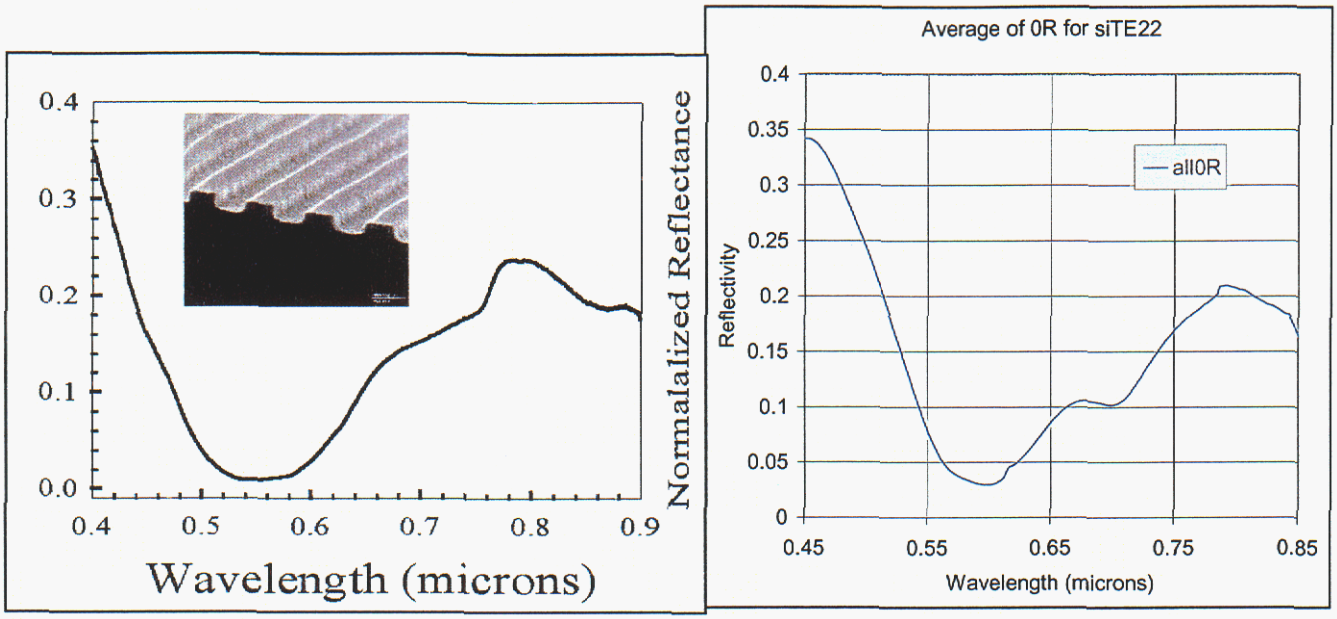

Figure 20. (left) Simulated average spectral reflectance curve representing all grating parameter combinations within the measurement: grating depth = 0.22-0.27 μm, grating pitch = 0.7 μm, and line width = 0.29-0.34 μm for TE incident light. (right) Measured .spectral reflectance curve of the same grating, normalized to a planar Si surface.

The simulated spectra (left) and the measured spectra (right) in Figure 20 appear to be in general agreement in both spectral feature location in the waveband and reflectivity values.

THIRD YEAR ACCOMPLISHMENTS

Solar Cell Development

The quality of low-cost multicrystalline-silicon (mc-Si) has increased to the point that its cell performance is close to that of single crystal (c-Si) cells, with the major difference resulting from the inability to texture mc-Si affordably. A low-cost, large-area, random, maskless texturing scheme independent of crystal orientation is expected to significantly impact the cost and performance of mc-Si photovoltaic technology. Web and ribbon-Si technologies also produce high-quality Si wafers, but as yet have not been able to introduce cost-effective cell texturing, which would provide a significant boost in their performance.

The innovation represented by this process lies in its ability to texture entire large-area mc-Si wafers at once. Other novel, wet-chemical approaches that work on some mc-Si materials are not effective on shiny web or ribbon materials because of their lack of nucleation sites. Because the RIE-texturing process removes several microns of material, it may also be used as a replacement for saw-damage removal etching, thereby simplifying and reducing the cost of the wafer preparation process.

Tri-crystalline silicon is a crystal compound of three mutually tilted mono-crystalline silicon grains. In contrast to the conventionally used single crystal silicon, the surface of all three grains is (110) oriented perpendicular to the growth direction. Using a tri-crystalline silicon seed, the ingot is grown using standard Cz techniques. Mechanical loading tests done on 150-μm thick wafers showed the maximum load strength of the tri-crystal wafers was 70% higher than that of single crystalline silicon. Preliminary production line data showed 5% better mechanical yield with tri-crystalline wafers compared to mono-Si of the same thickness.

Tri-crystalline Si wafers could produce cells with 5% higher yields than mono-Si due to their increased strength, but their use would require a replacement of the low-cost anisotropic wet texturing that works well only on single crystalline Si. The use of stronger wafers with improved light-trapping properties could allow thinner cells to be fabricated, thereby increasing the number of wafers produced per ingot by 60% and markedly reducing cell costs.

Other researchers reported the development of an RIE-texturing process using Cl_2 gas, which textures many wafers per batch, making it attractive for mass-production [1]. Using this process, they have produced a 17.1% efficient 225-cm^2 mc-Si cell, which is the highest efficiency mc-Si cell of its size ever reported. This shows that RIE texturing can be done without causing performance-limiting damage to Si cells. In this paper, we will discuss an RIE-texturing process that avoids the use of toxic and corrosive Cl_2 gas.

EXPERIMENTAL PROCEDURE

We developed several metal-catalyst assisted RIE-texturing techniques using SF_6/O_2 plasma chemistry in a Plasma-Therm 790 reactor. The cathode in the plasma chamber is constructed from graphite while the chamber walls and anode are made of aluminum. The textured surfaces exhibit reflectance of between 1 and 5 % for wavelengths below 1 μm without the benefit of anti-reflection films [2]. We investigated several texturing processes for different industrial mc-Si wafers to determine which produced the highest cell performance for various commercial fabrication sequences. We studied how to remove the plasma-induced contamination and surface damage without removing the benefits of the texture.

Previous work had shown that up to a 7% relative improvement in cell efficiency was obtained when two different RIE-texture processes were applied to groups of mc-Si wafers from BP Solar and compared with cells using planar control wafers from the same ingot [3]. In this paper, we will describe how these same two RIE-texture processes were applied to groups of tricrystalline (tri-c Si) wafers from Shell Solar. These groups were processed identically with two other groups of control wafers; one received their standard alkaline wet-texture process, one remained planar. Then all wafers were processed through their industrial cell production line using standard process schedules.

Shell Solar

The results of the initial experiment are shown in Table 5. Both of the RIE-textured cell groups outperformed the planar controls, especially the one using the conditioned texture. As Figure 21 shows, the improvement due to the conditioned texture is statistically significant.

Table 5. Average and Standard Deviation of Illuminated IV Parameters for 4 Groups of 102-cm^2 tri-crystalline Cells Processed at Shell

Front Surface Condition	Eff	V_{oc}	J_{sc}	FF
	%	mV	mA/cm^2	%
CONDITIONED TEXTURE	11.3	573	27.5	72
Std Dev.	0.3	4	0.4	1
Ti-ASSISTED	10.9	566	26.8	72
Std Dev.	0.4	6	0.7	1
PLANAR	10.7	565	26.9	71
Std Dev.	0.4	5	0.5	1
WET-TEXTURED	10.5	579	25.9	70
Std Dev.	0.7	10	0.9	3

Both groups of RIE-textured cells performed better than the planar cells, while the wet textured cells actually performed worse on average and had a higher degree of variability. To understand this, we performed Internal Quantum Efficiency (IQE) measurements on representative cells from each group. Results are shown in Figure 21.

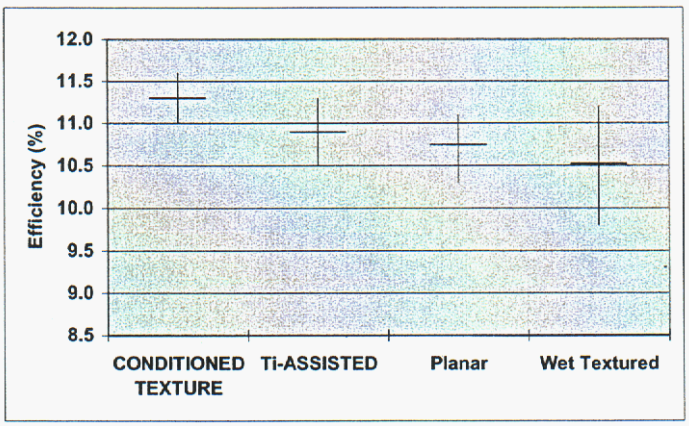

Figure 21. Average efficiency ± standard deviation for each of the 4 groups of cells. There were about 12 cells in each group.

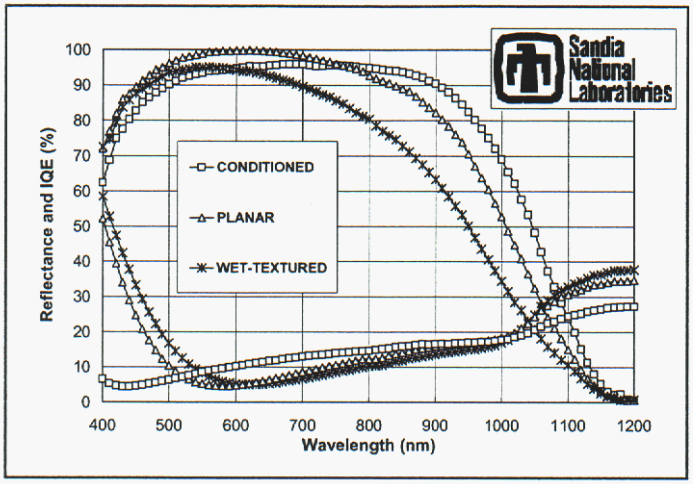

Figure 22. IQE and hemispherical reflectance of 3 tri-c Si cells with RIE-textured (conditioned texture), planar, or wet-textured front surfaces. All cells had otherwise identical processing, including single layer antireflection coating.

The IQE curves show that the RIE-textured cell has superior long-wavelength response compared to the planar cell, probably due to the oblique coupling of light into the cell, which increases carrier collection efficiency and promotes light trapping. However, the condition-textured cell does show a slight reduction in blue response, most likely due to residual RIE surface damage, even though an RCA-clean and nitric/HF damage removal etch (DRE) were performed after texturing. The solar-weighted reflectance of the RIE-textured cell is lower at 12.4%, compared to 13.3% for the planar cell and 13.8% for the wet-textured cell.

In contrast, the wet-textured cell shows a sharp decrease in long-wavelength response, possibly due to bulk defects introduced by subjecting the textured tri-c surface to subsequent high-temperature steps. In addition, the wet- texture actually appears to increase the surface reflectance somewhat. A photograph of the four types of cells compared in this experiment is shown in Figure 23.

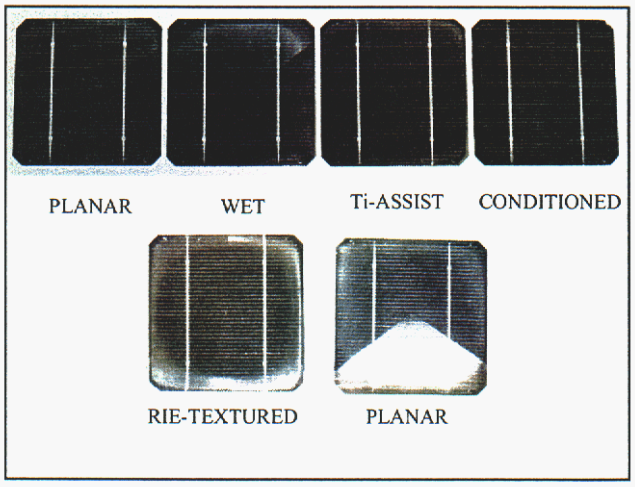

Figure 23. Top Row: Side-by-side photographs of cells from each group in experiment. Bottom Row: Conditioned and planar cells under high intensity light.

BP Solar

Previous work showed that an efficiency improvement of 2.5% could be obtained on RIE-textured BP Solar cells processed on their commercial production line [2]. We next studied whether the costly RCA-clean process was required for this performance improvement. We investigated cell response with and without an RCA clean, while using the identical conditioned texturing and nitric DRE processes. Results of this experiment are summarized in Table 6. We notice that incorporation of the RCA clean leads to a slight performance improvement relative to the no-RCA process, but the effect is statistically insignificant.

Table 6. Average Illuminated IV Parameters for 3 Groups of 130-cm^2 mc-Si Cells Processed at BP Solar

Cell Process	Eff(%)	J_{SC} (mA/cm^2)	V_{OC} (mV)	FF(%)
Controls	12.5	29.0	582	74.0
RCA	12.3	28.8	578	73.7
No-RCA	12.2	28.9	577	73.2

The cell results in Table 6 show that even with inclusion of the RCA clean and nitric DRE processes, the textured cell performance is still lower than that of the controls. Perhaps the nitric DRE process is not as effective on mc-Si surfaces as it was on tri-c Si. We therefore investigated alkaline-based DRE treatments. The results of the best alkaline-based DRE cells without RCA clean are summarized in Table 7. Since the wafers in this group were from the same material as those in Table 6, both planar and nitric DRE results from Table 6 are included for comparison.

Table 7. Solar Cell Performance using Different DRE Treatments.
No RCA clean was used after texturing.

Cell Process	Eff (%)	J_{SC} (mA/cm^2)	V_{OC} (mV)	FF (%)
Controls	12.48	28.99	582	74.0
Nitric DRE	12.19	28.86	577	73.2
Alkaline DRE	12.59	29.28	580	74.1

This demonstrates for the first time superiority of RIE-textured cells over planar controls without using the expensive RCA clean and nitric/HF DRE processes. Even though the efficiency and J_{SC} enhancements of the alkaline DRE process are rather modest at about 1.0 %, they suggest that a larger performance boost could be realized through optimization of the DRE and RIE-texture processes.

Figure 24 shows pictures of 130-cm^2 RIE textured cells with nitric/HF DRE treatments compared to a planar cell. The corner regions and areas near the edges are either planar or have yellowish texture. This non-black area typically covers 10-15-cm^2 of the 130-cm^2 cell area and negatively impacts cell performance. Improvement of the texture uniformity should significantly improve textured cell performance.

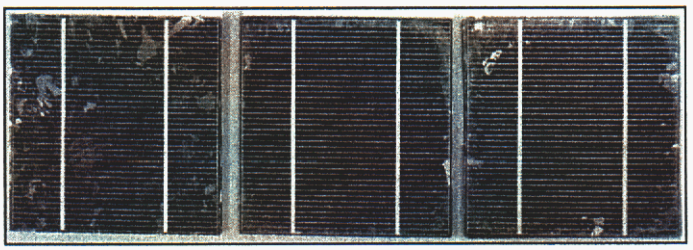

Figure 24. Side-by-side photograph of BP Solar cells. Left cell is planar, center and right cells are RIE-textured with nitric/HF DRE. All have commercial single layer ARC.

We have also examined the texture microstructure using scanning electron microscopy (SEM) following acid and alkaline-based DRE treatments. Figure 25 shows surface morphology after nitric acid DRE treatments of 20, 40 and 60 seconds. The effect of the DRE treatments is removal of all the nanoscale features even at the shortest duration of 20 sec. As etch times increase, only the largest feature dimensions survive, leaving structures with average dimensions in the 1-2 μm range. At the longest (60 sec) etch time, almost all of the sub-μm features are removed, leaving features with spacing in the 1-3 μm range.

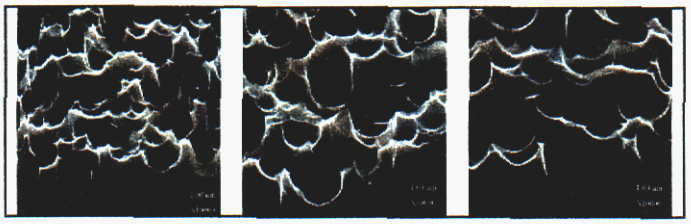

Figure 25. SEM micrographs of mc-Si surfaces after conditioned texture and nitric/HF DRE treatments of (a) 20 sec, (b) 40 sec, and (c) 60 sec.

We evaluated the absolute spectral reflectances of cells subjected to nitric DRE treatments of increasing duration. Figure 26 shows hemispherical reflectance measurements of three cells labeled a3, b2, and c2, as well as from a planar cell. All the solar cells had anti-reflection nitride films.

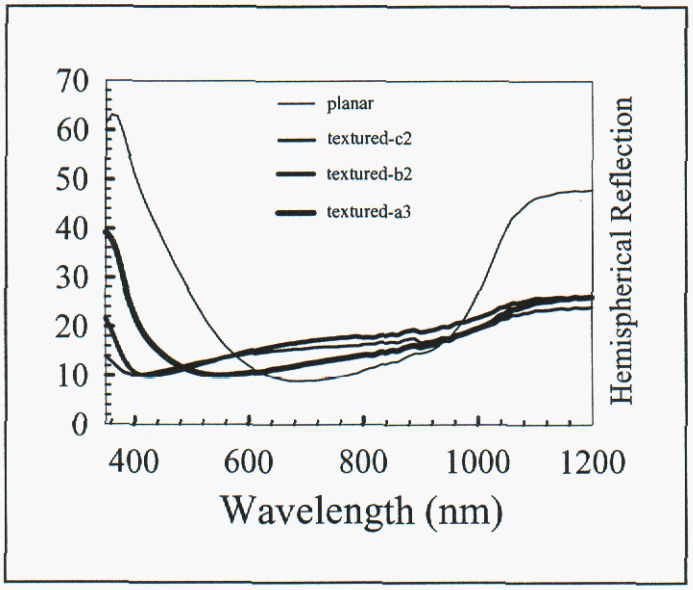

Figure 26. Absolute hemispherical spectral reflectance measurements of 4 BP Solar cells, including reflectance of gridlines. Cell c2 corresponds to Figure 25(a), b2 corresponds to 5(b), and a3 corresponds to 5(c).

Increasing the nitric/HF DRE time increases the reflectance at short wavelengths due to removal of sub-μm size features. However, lower reflectance in the important mid-solar wavelengths is obtained with the 60 sec DRE.

In comparison, Figure 27 shows surface morphology after alkaline DRE treatments of 20, 40 and 60 seconds. In contrast to nitric/HF etching, alkaline etching retains most of the fine structure. At 20 sec, surfaces are almost identical to as-fabricated RIE surfaces except for removal of sub-50 nm features. At 40 sec, the feature distribution is not that much different than that of the 20 sec DRE process. At 60 sec, almost all sub-μm features have been etched away, leaving an average spacing of about 1.0 μm and dimensions of 0.5 to 1.0 μm.

Figure 27. SEM micrographs of mc-Si surfaces after conditioned texture and alkaline DRE treatments of (a) 20 sec, (b) 40 sec, and (c) 60 sec.

Ebara Solar

We were successful in developing an RIE-texturing process that produced low reflectance surfaces on shiny web-Si materials from Ebara Solar. Reflectance curves from 2 textured web blanks and a co-processed FZ wafer are compared with that of a planar web wafer in Figure 28.

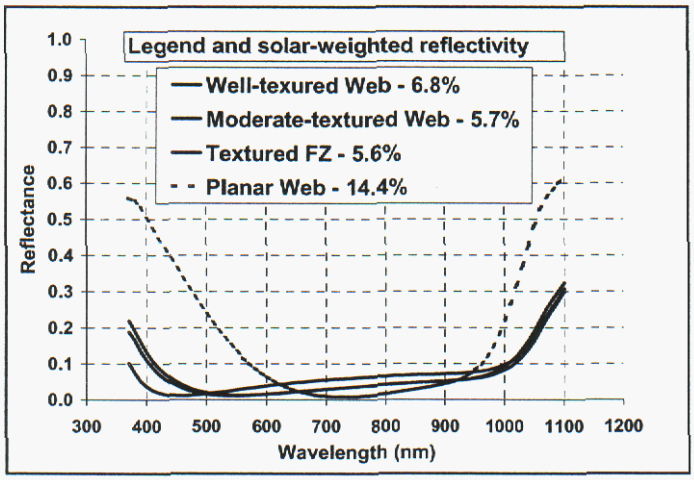

Figure 28. Surface reflectivity with SiNx AR coating of RIE textured cells (before grid metallization).

Although the co-processed FZ cell showed slight long-wavelength improvement, the web cells suffered from severe bulk-lifetime degradation. This could possibly be due to stresses in the web that result in bulk defects when the textured material is subjected to subsequent high-temperature steps. Work on these commercial materials is ongoing and will be reported later.

Discussion

Both of the RIE-textured Shell tri-c Si cell groups outperformed the standard planar controls by up to 6%, while wet-textured cells actually performed worse. If tricrystal cells are used in production to increase yields and reduce costs, RIE-texturing should be able to boost their performance.

The BP Solar cells showed a small 1% gain in efficiency without the use of an expensive post-texture RCA clean. This shows potential for the use of RIE-texturing as a replacement for saw-damage removal etching in order to maintain efficiencies when cells are made thinner. This would increase the number of wafers produced per ingot significantly and markedly reduce cell and module costs.

We developed a maskless plasma texturing technique for multicrystalline Si (mc-Si) cells using Reactive Ion Etching (RIE) that results in higher cell performance than that of standard untextured cells. Elimination of plasma damage has been achieved while keeping front reflectance to low levels. Internal quantum efficiencies higher than those on planar and wet-textured cells have been obtained, boosting cell currents and efficiencies by up to 6% on tricrystalline Si cells.

Plasma Process Modeling

The major process-modeling goal for this year was to improve the utility of the SURFMOD code, which was developed in previous years under this LDRD. This code simulates the roughening of an initially smooth surface during exposure to an aggressive processing environment such as a plasma. Last year SURFMOD was developed to the point that it could simulate some features of the roughening process in moderate agreement with the texturing results from the experimental part of this project. The simulations require the identification of etching mechanisms and the flux of etchant species to the surface. SURFMOD, as developed last year required *ad hoc* specification of the mechanism and fluxes. However, Sandia has code (AURORA) developed for modeling the chemistry of these plasmas and this was used successfully in the early stages of this program to develop the etch mechanism and to simulate the plasma etch process. We also have code (ICARUS) for direct simulation of 2-D plasma etch. Neither code can simulate topological development on the nano-scale (or on any scale) needed to model the blackening of silicon. This year, development of SURFMOD focused on the integration of these other plasma codes, AURORA and ICARUS, so that the user can simulate the surface morphological development in a seamless way using the three codes. SURFMOD was augmented to allow the use of CHEMKIN input formats, consistent with the other plasma codes. Thus, when AURORA has been used to develop a chemical mechanism consistent with observed etch rates, the mechanism can be directly imported into SURFMOD and used as the etch mechanism to predict surface texturing. In effect, the mechanism developed with AURORA specifies precisely what an incident gas phase molecule will do on the surface and SURFMOD uses this information to predict surface structural changes.

The integration of the code ICARUS with SURFMOD is not complete. ICARUS gives a full description of the transport of gas phase species to the surface: flux, energy, and angular distributions. SURFMOD needs this information to couple with the mechanism provided from AURORA. Several issues connected with coordination of the 2-D non-regular gridding of ICARUS and the 3-D mesh of SURFMOD remain to be resolved before development of SURFMOD is complete and the code can advance to the verification and validation stage. We anticipate that, with the completion of this LDRD, the development and testing of SURFMOD will be completed using other (ASCI) resources.

Optical Modeling

Triangular and Trapezoidal Silicon Gratings: Determination of Duty Cycle from Measured Data

From SEM photographs of the gratings a rough estimate of the grating depth and duty cycle may be deduced. These estimates were used as starting points for determining the values for these parameters in Gsolver that best fit the measured data. It was found that a trapezoidal grating shape, although only slightly skewed from a rectangle, offered much better agreement with the measured data. Similarly, a narrow triangle agreed with the measurements better than a standard triangular grating where the entire grating period is encompassed by the base of the triangle. All calculations assume incident light at an angle of 7 degrees. Fifteen orders were carried through the rigorous coupled wave analysis using the Gsolver program.

Triangular Grating

The triangular grating was approximated with a four-level grating as shown in Figure 28. From the SEM photograph it appeared that the period was roughly 1.0μm, with the base of the triangular grating not extending the full period. The grating depth was also approximated from the SEM photograph. However, the period and etch-depth cannot be determined exactly from the photograph. To compensate for this, several grating periods were simulated. The best match between calculated and measured values occurred with a grating period of 0.9μm.

In a similar manner, the etch depth cannot be measured exactly from the SEM photograph, moreover variations in etch depth occur across the wafer. For this reason an average of data at two depths were used to compare to the measured data. Two grating depths, 0.6μm and 0.7μm, were averaged together for the calculated curves seen in Figures 29 and 30.

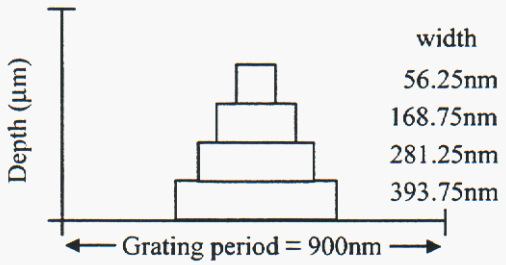

Figure 28. Triangular grating approximation.

With the exception of variations at longer wavelengths, the calculated and measured data correlate well.

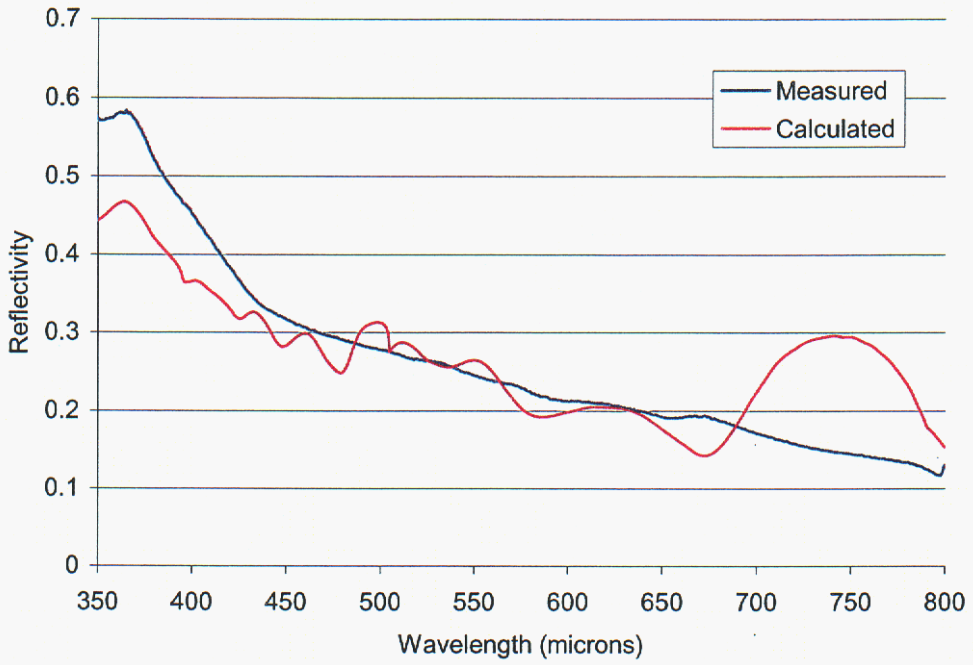

Figure 29. Triangular grating TE reflectivity.

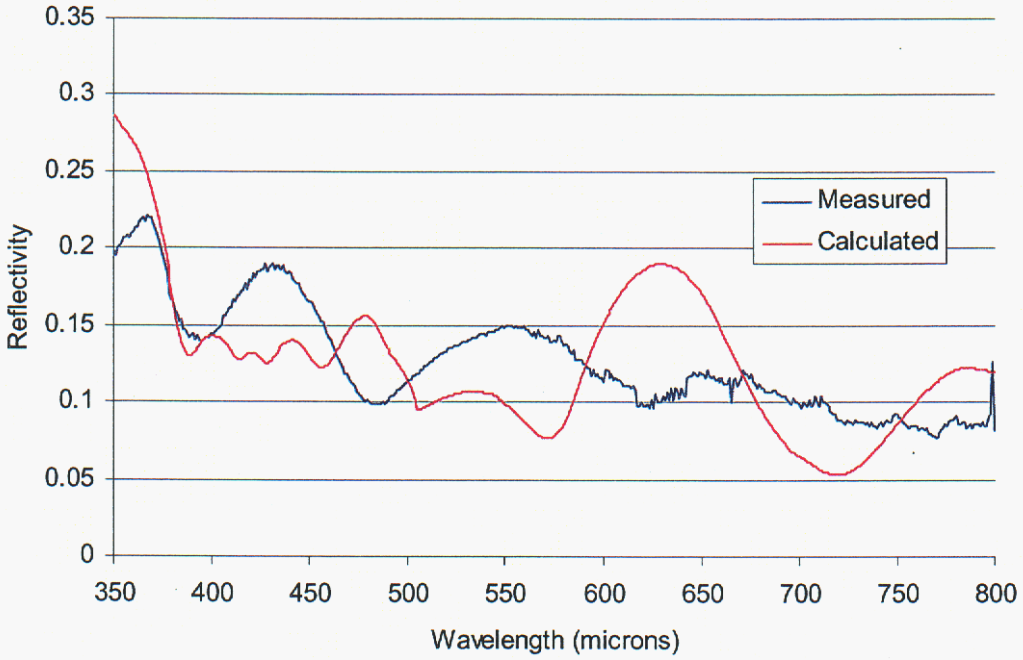

Figure 30. Triangular grating TM reflectivity.

Trapezoidal Grating

The trapezoidal grating was approximated in a similar manner to the triangular grating. Four levels were again used as shown in Figure 31. The trapezoidal nature of the grating is such as to almost be rectangular. Again rough estimates of the grating depth and period were taken from an SEM photograph. From these approximations a range of periods were again simulated at various etch depths. Again the best match in data occurred for a grating period of 0.9μm. As for the triangular case the grating depth was averaged over two values to incorporate the variation across the grating. Depths of 0.9 μm and 1.0μm were used. Calculated and measured data align quite well.

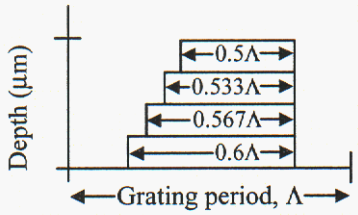

Figure 31. Trapezoidal grating approximation

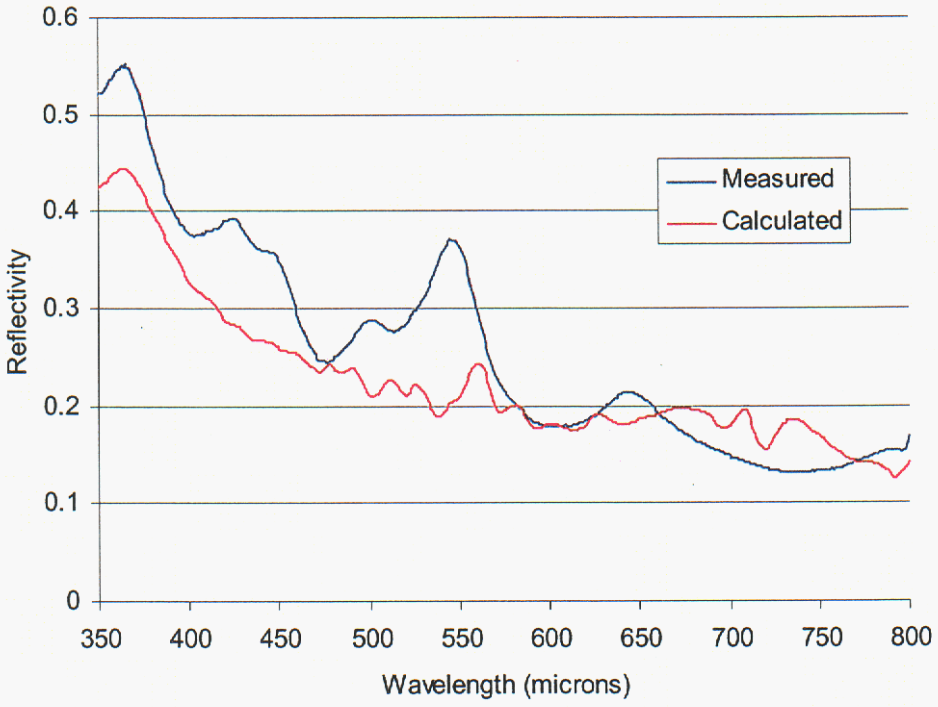

Figure 32. Trapezoidal grating TE reflectivity

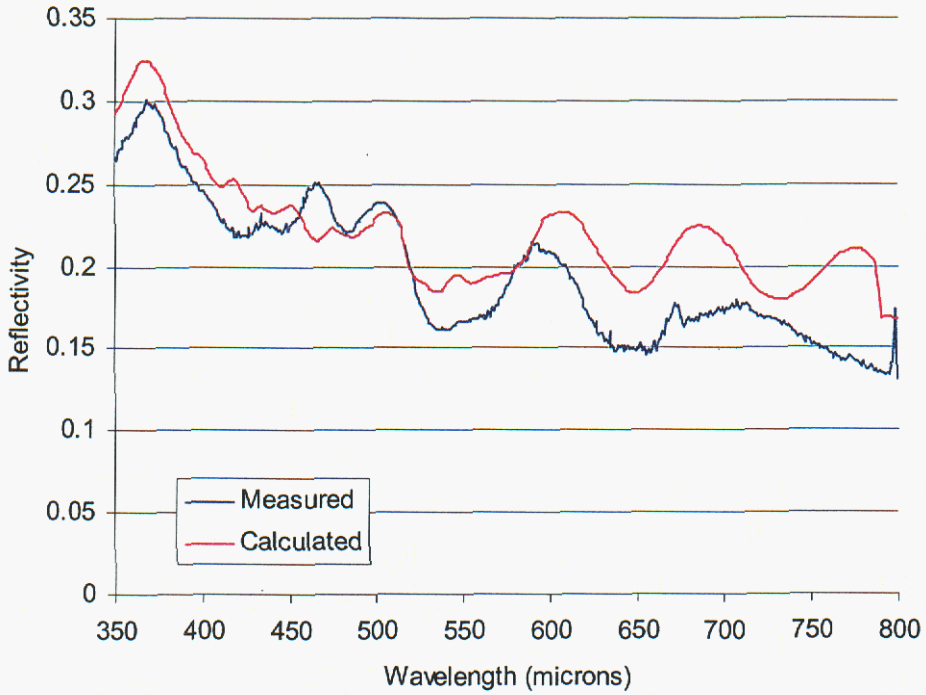

Figure 33. Trapezoidal grating TM reflectivity.

Symmetric Trapezoidal Grating Reflectivity

The trapezoidal grating was simulated again, this time with a symmetric profile as seen in Figure 34. Four levels were again used. Depths of 0.9 μm and 1.0μm were used. As expected there is almost no difference from the trapezoidal grating simulated before.

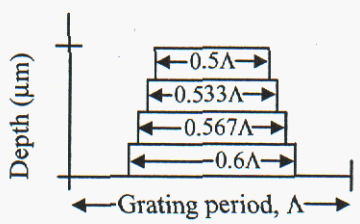

Figure 34. Trapezoidal grating approximation.

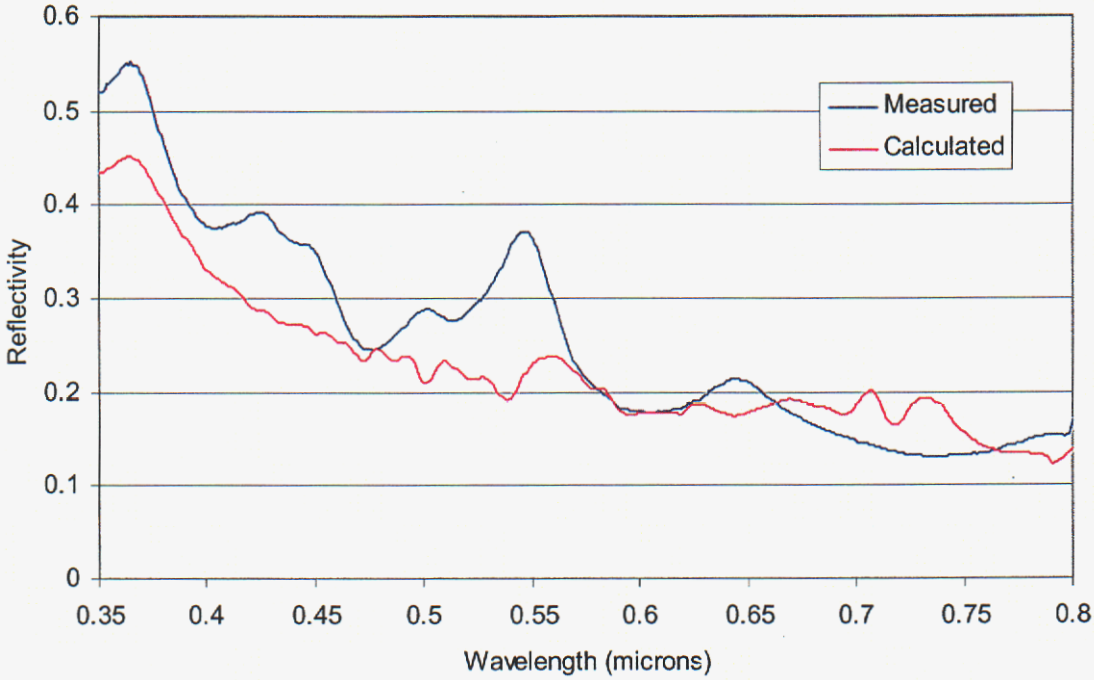

Figure 35. Symmetric trapezoidal grating TE reflectivity.

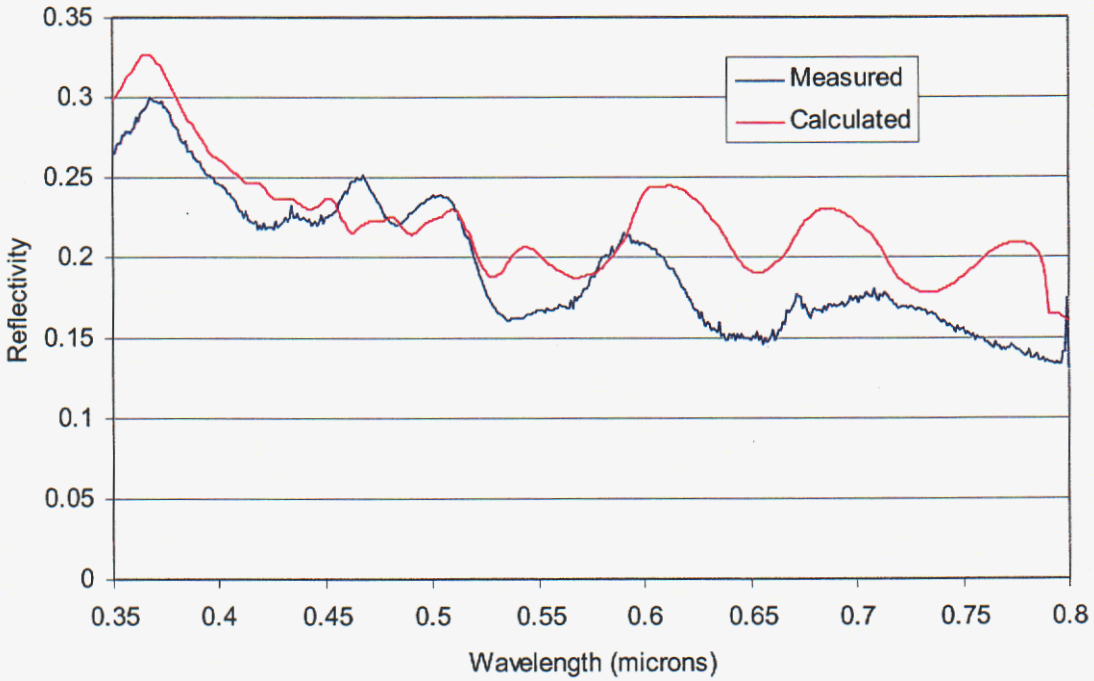

Figure 36. Symmetric trapezoidal grating TM reflectivity.

Triangular Grating Measurements and Calculations

Figure 37 shows scanning electron microscope pictures of triangular profile gratings etched in Si using RIE. The triangular structures shown in Figure 37 are characterized by periods of ~ 670 (left) and ~ 420 nm (right) with full width at half-maximum depths (FWHM) at ~ 300 nm and 100 nm respectively. Grating depths respectively are 800 and 500 nm.

Figure 38 shows absolute hemispherical reflectance measurements (using randomly polarized light) from the triangular gratings shown in Figure 37.

Figure 39 shows the average calculated reflectance from four gratings in the range of the grating at left in Figure 37. The four gratings used were as follows d = grating depth, Λ = period:

1) d = 0.7μm, Λ = 0.64μm
2) d = 0.7μm, Λ = 0.7μm
3) d = 0.8μm, Λ = 0.64μm
4) d = 0.8μm, Λ = 0.7μm

Figure 40 shows the average calculated reflectance from four gratings in the range of the grating at right in Figure 37. The four gratings used were as follows d = grating depth, Λ = period:

1) d = 0.5μm, Λ = 0.4μm
2) d = 0.6μm, Λ = 0.4μm
3) d = 0.5μm, Λ = 0.42μm
4) d = 0.6μm, Λ = 0.42μm

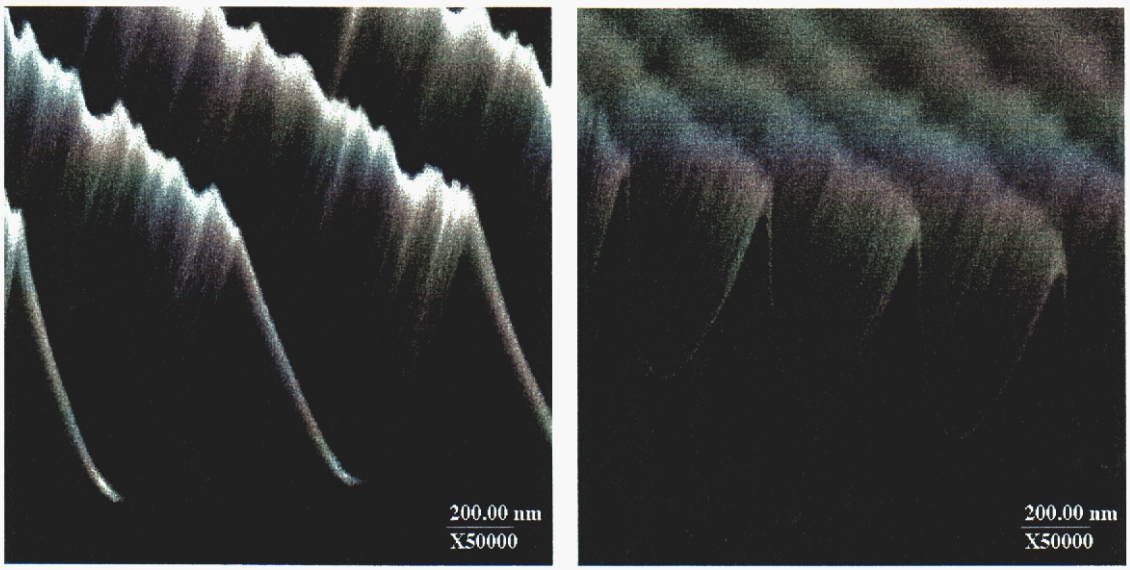

Figure 37. SEM pictures of 670-nm period (left) and 420-nm (right) Si gratings fabricated using RIE.

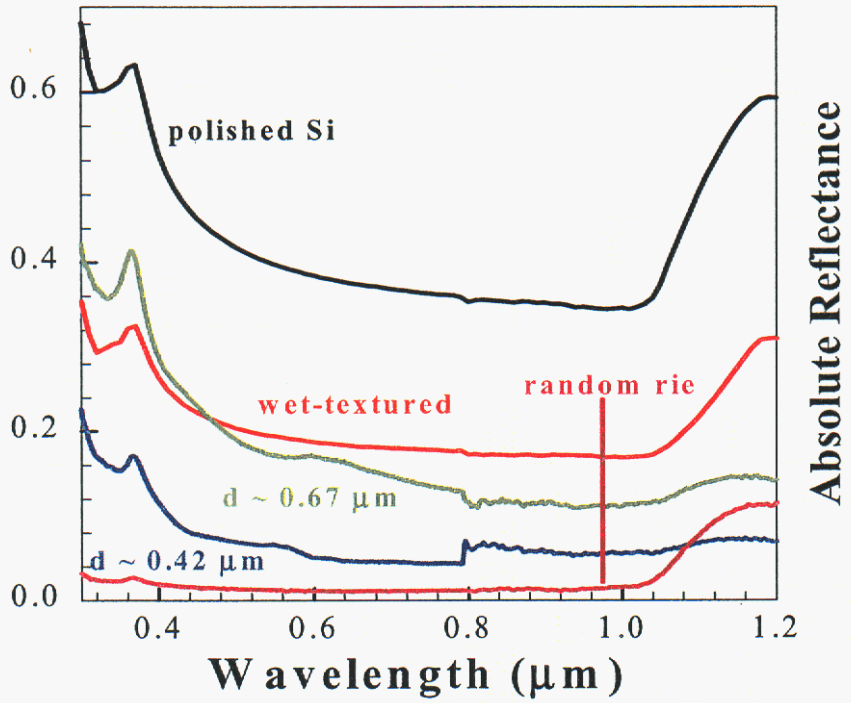

Figure 38. Hemispherical reflectance measurements from triangular profiled, 1D gratings shown in Figure 37.

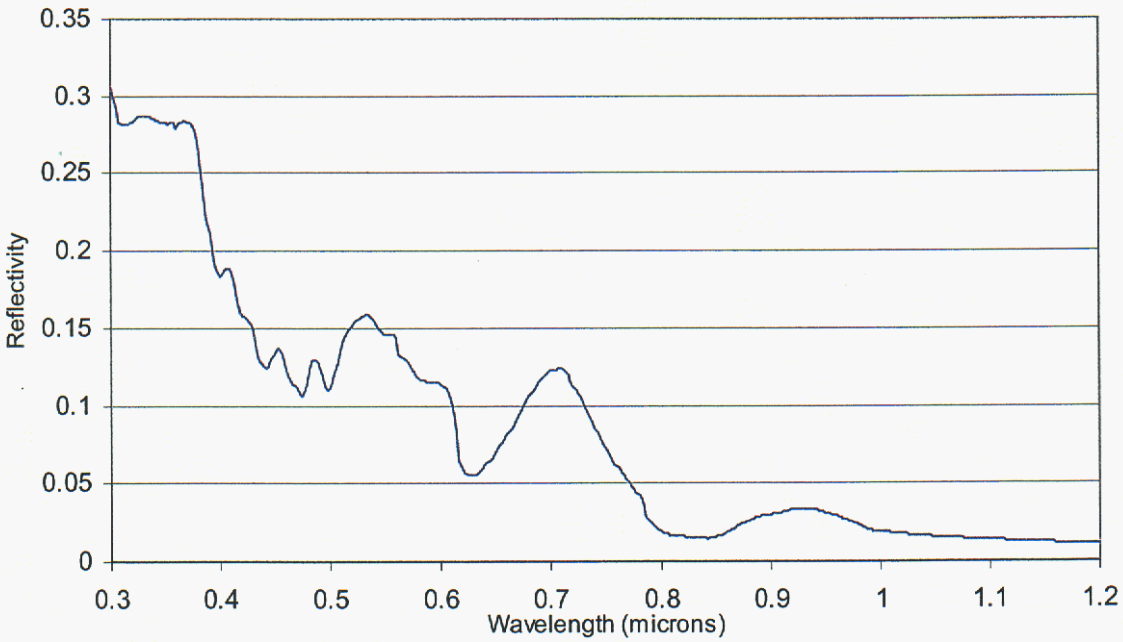

Figure 39. Calculated reflectivity for triangular grating with nominal 0.67µm period.

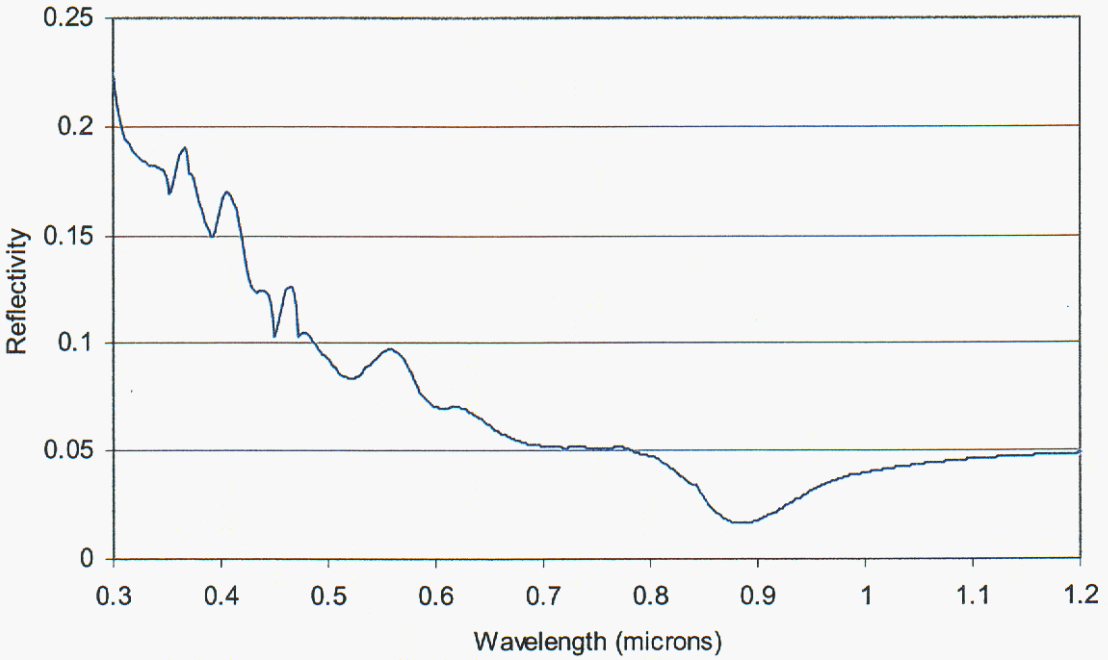

Figure 40. Calculated reflectivity for triangular grating with nominal 0.42μm period.

Modeling of Reflectivities of Gratings on Silicon Wafers

Numerical modeling of surface-relief single-spatial frequency silicon gratings has been performed using rigorous coupled wave analysis to determine if experimental results of one-dimensional gratings on silicon can be verified and possibly predicted. Reflected light was experimentally measured using a hemispherical reflectance system modified so that the polarization of the incident light was well known. Across the surface of the wafer there are variations in the duty cycle and depth of the gratings. Since the measured data was taken over a relatively large area, the data is an average of the grating depths and duty cycles found over this region. As a result, one set of grating parameters will not match the experimental data; therefore, an averaging method was used.

From SEM photographs of the gratings a rough estimate of the grating depth and duty cycle may be deduced. These estimates were used as starting points for determining the values for the modeling parameters that best fit the measured data. Modeling only the one estimate for depth and duty cycle results in plots of reflectivity versus wavelength with much finer features than the experimental data. This is to be expected as the measured data is averaged over an area with varying grating conditions.

An average was taken of the calculated data around the central point in order to smooth the curves. A range was chosen for the depth and duty cycle such that the feature shapes of the averaged calculated reflectivity as a function of wavelength closely resembled those of the experimental plot. In general, wider ranges lead to greater smoothing of the calculated curves when the four points are averaged.

In all cases good agreement between the experimental and calculated curves could be obtained for both TE and TM data sets. An example appears in Figure 41. The method appears to work well for matching experimental data. However, whether the method will work for predicting experimental results is less

certain. If the range chosen for the averaging in the numerical modeling can be matched to the fabrication tolerances of the grating, then it could be expected that a similar agreement between the data could be obtained.

In summary, calculated reflectivities of one-dimensional (linear) gratings with a single pitch and depth result in overall reflectivity values that resemble those measured, but with finer features. Small variations in these input parameters change, sometimes significantly, the placement and amplitude of these fine features. Moreover, the fabrication process cannot reproduce a single pitch or depth so that the measured grating response is an integrated result over several pitches and depths. Therefore, while we can ***confirm*** measured grating responses by propitiously averaging a set of calculated grating responses, as above, this method would **not** be an appropriate ***predictor*** of grating response until the fabrication process results in a more uniform grating.

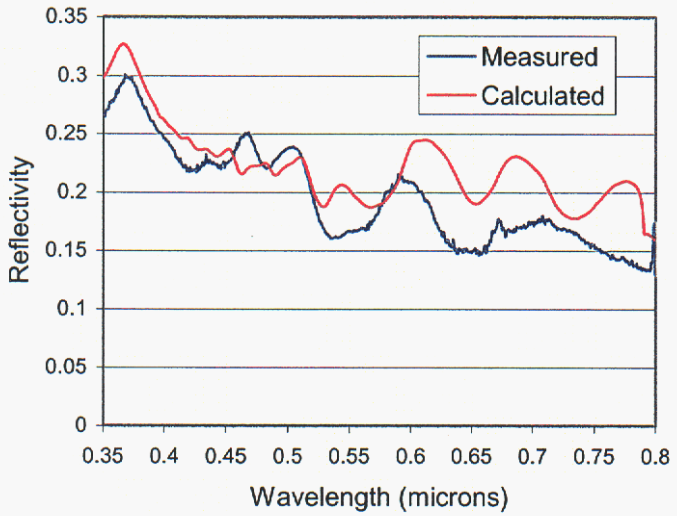

Figure 41. Trapezoidal grating TM reflectivity.

ACKNOWLEDGEMENTS

We would like to thank Sandia National Laboratories LDRD program for their financial support during the course of this work. In particular, we would like to thank James M. Gee, Jeannette Moore, and Bev Silva of Sandia for their help during the course of this project. The authors would like to thank Tim Koval at BP Solar for cell processing. Many thanks go to Barry Hansen at Sandia for the cell measurements. We would also like to thank the Center for High Technology Materials at the University of New Mexico for use of their clean room facilities. Thanks are also to Richard Marquardt and Sam McCormack of Gratings, Inc. for their assistance.

REFERENCES

[1] Inomata, Y., Fukui, K., Shirasawa, K., 1997, "Surface Texturing of Large Area Multicrystalline Si Solar Cells Using Reactive Ion Etching Method," *Solar Energy Mat. Solar Cells,* **48**, Part II, pp 237-242.

[2] Ruby, D. S., Zaidi, S. H., Narayanan, S., "Plasma-Texturization for Multicrystalline Silicon Solar Cells," *Twenty-Eighth IEEE PVSC*, 2000, pp. 75-78.

[3]. Ruby, D. S., Zaidi, S. H., Damiani, B. M., Rohatgi, A., "RIE-Texturing of Multicrystalline Silicon Solar Cells," *PVSEC-12*, Jeju, Korea, June 2001, pp. 273-274.

DISTRIBUTION

Keith Matthei
GT Solar Technologies
472 Amherst Street
Nashua, NH 03063

Gary Stevens
Matrix Solar
7500 Meridian Place
Albuquerque, NM 87121

Mike Nowland
Spire Corporation
One Patriots Park
Bedford, MA 01810

Steve Hogan
Spire Corporation
One Patriots Park
Bedford, MA 01810

Juris Kalejs
ASE Americas, Inc.
Four Suburban Park
Billerica, MA 01821-3980

Mark Rosenblum
ASE Americas, Inc.
Four Suburban Park
Billerica, MA 01821-3980

James Rand
AstroPower
Solar Park
Newark, DE 19716-2000

Chandra Khattak
Crystal Systems
27 Congress Street
Salem, MA 01970

Mohan Narayanan
BP Solar
630 Solarex Court
Frederick, MD 21701

John Wohlgemuth
BP Solar
630 Solarex Court
Frederick, MD 21701

Ted Ciszek
National Renewable Energy Lab
1617 Cole Blvd.
Golden, CO 80401-3393

Bhushan Sopori
National Renewable Energy Lab
1617 Cole Blvd.
Golden, CO 80401-3393

Jack Hanoka
Evergreen Solar
259 Cedar Hill St.
Marlboro, MA 01752

Andrew Gabor
Evergreen Solar
259 Cedar Hill St.
Marlboro, MA 01752

Paul Ciszek
Evergreen Solar
259 Cedar Hill St.
Marlboro, MA 01752

Theresa Jester
Shell Solar
P. O. Box 6032
Camarillo, CA 93011

Dan Meier
Ebara Solar, Inc.
13 Airport Road
Belle Vernon, PA 15012

Satoshi Yamanaka
EBARA Solar, Inc.
13 Airport Road
Belle Vernon, PA 15012

Ajeet Rohatgi
University Center of Excellence for
Photovoltaics
Georgia Institute of Technology
School of Electrical Engineering
777 Atlantic Drive
Atlanta, GA 30332-0250

Jeffrey Mazer
US Department of Energy, EE-11
1000 Independence Ave., SW
Washington, DC 20585

Richard King
US Department of Energy, EE-11
1000 Independence Ave., SW
Washington, DC 20585

Richard Swanson
SunPower Corporation
430 Indio Way
Sunnyvale, CA 94086

Bob Hassett
US Department of Energy, EE-11
1000 Independence Ave., SW
Washington, DC 20585

Dan Ton
US Department of Energy, EE-11
1000 Independence Ave., SW
Washington, DC 20585

Ruben Balanga
Shell Solar
P. O. Box 6032
Camarillo, CA 93011

Bob Hall
AstroPower
Solar Park
Newark, DE 19716-2000

Saleem Zaidi
Gratings, Inc.
2700-B Broadbent Pkwy. NE
Albuquerque, NM 87107

Hong Hou
EMCORE Photovoltaics
10420 Research Rd. S.E.
Albuquerque, NM 87123

Richard King
Spectrolab, Inc.
12500 Gladstone Avenue
Sylmar, CA 91342-5373

Frank Ho
Emcore, Inc.
15251 E. Don Julian Road
City of Industry, CA 91745

Vahan Garboushian
Amonix, Inc.
3425 Fujita Street
Torrance, CA 90505

Tihu Wang
National Renewable Energy Lab
1617 Cole Blvd.
Golden, CO 80401

Dave Smith
SunPower Corporation
430 Indio Way
Sunnyvale, CA 94086

Bob McConnell
National Renewable Energy Lab
1617 Cole Blvd.
Golden, CO 80401

0752	Doug Ruby, 6218
0752	James Gee, 6216
0752	David King, 6218
0753	Joe Tillerson, 6218
0836	Rick Buss, 9117
0603	Shanalyn Kemme, 1743
0188	Donna Chavez, 1011
0753	PV Library (C. Brooks) (5 copies)
0899	Technical Library, 9616 (2 copies)
0612	RA Desk, 9612 for DOE/OSTI
9018	Central Technical Files, 8945-1